LAWRENCE
LIVERMORE
NATIONAL
LABORATORY

LLNL-JRNL-405733

# Investigation of Rayleigh-Taylor turbulence and mixing using direct numerical simulation with experimentally-measured initial conditions. I. Comparison to experimental data

N. Mueschke, O. Schilling

July 28, 2008

Physics of Fluids

## Disclaimer

This document was prepared as an account of work sponsored by an agency of the United States government. Neither the United States government nor Lawrence Livermore National Security, LLC, nor any of their employees makes any warranty, expressed or implied, or assumes any legal liability or responsibility for the accuracy, completeness, or usefulness of any information, apparatus, product, or process disclosed, or represents that its use would not infringe privately owned rights. Reference herein to any specific commercial product, process, or service by trade name, trademark, manufacturer, or otherwise does not necessarily constitute or imply its endorsement, recommendation, or favoring by the United States government or Lawrence Livermore National Security, LLC. The views and opinions of authors expressed herein do not necessarily state or reflect those of the United States government or Lawrence Livermore National Security, LLC, and shall not be used for advertising or product endorsement purposes.

# Investigation of Rayleigh–Taylor turbulence and mixing using direct numerical simulation with experimentally-measured initial conditions. I. Comparison to experimental data

Nicholas J. Mueschke*
*Department of Mechanical Engineering, Texas A&M University, College Station, Texas 77843*

Oleg Schilling†
*Lawrence Livermore National Laboratory, Livermore, California 94550*

(Dated: July 11, 2008)

A $1152 \times 760 \times 1280$ direct numerical simulation (DNS) using initial conditions, geometry, and physical parameters chosen to approximate those of a transitional, small Atwood number Rayleigh–Taylor mixing experiment [Mueschke, Andrews and Schilling, J. Fluid Mech. **567**, 27 (2006)] is presented. The density and velocity fluctuations measured just off of the splitter plate in this buoyantly unstable water channel experiment were parameterized to provide physically-realistic, anisotropic initial conditions for the DNS. The methodology for parameterizing the measured data and numerically implementing the resulting perturbation spectra in the simulation is discussed in detail. The DNS model of the experiment is then validated by comparing quantities from the simulation to experimental measurements. In particular, large-scale quantities (such as the bubble front penetration $h_b$ and and the mixing layer growth parameter $\alpha_b$), higher-order statistics (such as velocity variances and the molecular mixing parameter $\theta$), and vertical velocity and density variance spectra from the DNS are shown to be in favorable agreement with the experimental data. Differences between the quantities obtained from the DNS and from experimental measurements are related to limitations in the dynamic range of scales resolved in the simulation and other idealizations of the simulation model. This work demonstrates that a parameterization of experimentally-measured initial conditions can yield simulation data that quantitatively agrees well with experimentally-measured low- and higher-order statistics in a Rayleigh–Taylor mixing layer. This study also provides resolution and initial conditions implementation requirements needed to simulate a physical Rayleigh–Taylor mixing experiment. In Part II [Mueschke and Schilling, Phys. Fluids (2008)], other quantities not measured in the experiment are obtained from the DNS and discussed, such as the integral- and Taylor-scale Reynolds numbers, Reynolds stress anisotropy and two-dimensional density and velocity variance spectra, hypothetical chemical product formation measures, other local and global mixing parameters, and the statistical composition of mixed fluid.

PACS numbers: 47.20.-k, 47.20.Ma, 47.27.-i, 47.27.Cn, 47.27.E-, 47.27.ek, 47.27.wj, 47.11.Bc, 47.11.Kb

## I. INTRODUCTION

Numerical simulations have emerged as a powerful approach to understanding the detailed dynamics of Rayleigh–Taylor instability-induced turbulence and mixing. In particular, simulations have complemented experiments by providing detailed data, which may not be otherwise accurately measured. Early studies used monotone-integrated large-eddy simulation (MILES),[1–5] in which intrinsic numerical dissipation in the algorithm provided an effective dissipation at the small scales. However, the results depended on the grid resolution, with higher resolutions corresponding to larger numerical (rather than physical) Reynolds numbers. As a result, molecular transport, dissipation, and diffusion effects were not taken into account. More recently, massively-parallel computing has enabled well-resolved direct numerical simulations (DNS) of Rayleigh–Taylor instability and mixing.[6–10] For a given kinematic viscosity and mass diffusivity, all of the scales can be resolved provided sufficient grid resolution. Such simulations explicitly account for molecular dissipation and diffusion effects. Large-eddy simulations (LES) using explicit subgrid-scale models have not been extensively applied to Rayleigh–Taylor flows,[11–14] as the resolution requirements are nearly as large as for DNS, and the dependence of quantities obtained from the LES on the functional form and parameters of the subgrid-scale model is not yet fully understood.

While a relatively large number of MILES of Rayleigh–Taylor instability and mixing has been performed, there are comparatively many fewer DNS available due to the high resolution requirements. In addition, the vast majority of simulations performed considered idealized choices of simplified initial conditions arising from *assumed* spectra of interfacial (density) and/or velocity perturbations. Specifically, fluids with arbitrarily chosen densities, molecular dissipation and diffusion coefficients, and initial perturbation spectra are most often used in these simulations for convenience. Typically, these studies are focused on fundamental investigations of the mixing properties, including asymptotic-time (self-similar) scalings of bubble and spike front penetrations, mixing fractions, evolution of energy spectra, and other statistics.[5–8,10] An ancillary focus of many of these investigations is whether the late-time flow properties depend on the specific form of the initial conditions.[10,15] Only a few simulations to date have considered these questions using initial conditions and other simulation parameters relevant to physical experiments,[3,4,16] although all of these studies have used MILES. However, compromises were also made in each case (with only a partial treatment of physical parameters or initial conditions), often dictated by limitations in the numerical algorithm or experimental measurements.

---

*Present address: Southwest Research Institute, San Antonio, Texas 78238

†Author to whom correspondence should be addressed: `schilling1@llnl.gov`.

In a broader context, the present work is motivated by the challenge of developing a more physically-realistic numerical model of a Rayleigh–Taylor instability experiment, from which information not available from the experimental measurements and novel insights into the physics and modeling of such flows, may be obtained. In particular, the feasibility and utility of using initial conditions measured experimentally[17] to seed a miscible, small Atwood number, turbulent Rayleigh–Taylor mixing layer is demonstrated in this work. The method of implementing experimentally-measured initial conditions is validated by comparing various quantities from the DNS to experimental measurements, including integral-scale statistics, higher-order statistics, molecular mixing parameters, and energy spectra. This detailed comparison of quantities provides confidence in the simulation model, as well as guidance for future simulations that could potentially provide even better agreement with the experimental data. Other quantities obtained from the DNS, that are not readily available from experimental measurements, are also interpreted in Part II.[18] It is noteworthy that all previously reported DNS of Rayleigh–Taylor mixing have used a Schmidt number of unity: the present DNS is the first reported simulation (DNS or LES) of Rayleigh–Taylor instability and mixing with a Schmidt number different from unity.

This paper is organized as follows. Previous three-dimensional simulations of variable-density multi-mode incompressible turbulent Rayleigh–Taylor mixing are summarized in Sec. II, together with a brief summary of their specification of initial conditions. The methodology for parameterizing the initial conditions from the water channel Rayleigh–Taylor mixing experimental measurements is discussed in detail in Sec. III with additional details provided in the Appendix. The numerical methods used for the direct numerical simulation are summarized in Sec. IV. Quantities from the DNS using the parameterized initial conditions are directly compared to the corresponding quantities obtained from the experiment in Sec. V. Finally, a summary of the principal findings and conclusions are given in Sec. VI.

## II. PREVIOUS THREE-DIMENSIONAL SIMULATIONS OF MULTI-MODE INCOMPRESSIBLE VARIABLE-DENSITY RAYLEIGH–TAYLOR MIXING

A brief summary of previous three-dimensional simulations of multi-mode miscible incompressible Rayleigh–Taylor mixing with a discussion of initial conditions used is presented here. Examples of initializations using fully isotropic initial conditions are given. In addition, initial conditions modeling used in several Rayleigh–Taylor instability simulations that use information obtained from experimental measurements or qualitative experimental data is briefly discussed.

### A. Introductory remarks regarding initial conditions

Many numerical simulations of Rayleigh–Taylor mixing have been performed to study the growth rate of turbulent mixing layers at various Atwood numbers. Much of this work has focused on examining the late-time, self-similar turbulent growth regime, and less effort has been given to simulations representing physical experiments. As a result, most three-dimensional simulations are initialized with small *ad hoc*, isotropic perturbations to the initial interface or density field. Few simulations have used experimentally-measured initial conditions and, no *direct numerical simulation* of a turbulent Rayleigh–Taylor experiment has been reported to date. Table I lists representative pertinent multi-mode, miscible Rayleigh–Taylor simulations, their numerical techniques, and types of interfacial and velocity perturbation initial conditions used. Previous simulations also assumed unity Schmidt number, rather than a physical value, as well as arbitrary values of the viscosities of the constituent fluids.

The DNS presented here differs from the other numerical simulations in Table I in that the initial conditions are taken from measured initial perturbations in both the $x$- and $y$-directions (perpendicular to the direction of gravity) in a Rayleigh–Taylor mixing experiment.[17] *No assumption of isotropy* is made in the present work. While separate interfacial perturbation spectra are applied in the $x$- and $y$-directions, the methods used here are similar to the commonly used initialization methods with azimuthally-averaged (*i.e.* isotropic) energy spectra.[2,5,6,16] In wave number space, the current initialization of the interfacial perturbations limits fluctuations only to those modes aligned with the $x$- and $y$-axes. This differs from isotropic initializations where azimuthal rings of radius $k = \sqrt{k_x^2 + k_y^2}$ are populated with energetic modes. Thus, for the mixing layer considered here, energy that develops in wave numbers not aligned with the $x$- and $y$-axes results from nonlinear interactions of bubbles and spikes. Note that initial interfacial (density) *and* velocity perturbations are simultaneously present in

| | Numerical technique | Interfacial perturbation | Velocity perturbation |
|---|---|---|---|
| Youngs[1,2] | MILES | isotropic | – |
| Linden et al.[3] | MILES | isotropic | – |
| Dalziel et al.[4] | MILES | isotropic | anisotropic (measured) |
| Cook and Dimotakis[6] | DNS | isotropic | – |
| Cook and Zhou[7] | | | |
| Cabot and Cook[8] | | | |
| Young et al.[9] | DNS | isotropic | – |
| Cook et al.[13] | LES | isotropic | – |
| Ristorcelli and Clark[10] | DNS | isotropic | – |
| Ramaprabhu and Andrews[16] | MILES | isotropic (measured) | – |
| Ramaprabhu and Andrews[16] | MILES | – | isotropic (measured) |
| Dimonte et al.[5] | MILES | isotropic | – |
| Cabot[14] | LES | isotropic | – |
| Present work | DNS | anisotropic (measured) | anisotropic (measured) |

TABLE I: Summary of previous and current three-dimensional simulations of multi-mode, miscible Rayleigh–Taylor instability and mixing. The numerical technique (DNS: direct numerical simulation; LES: large-eddy simulation; MILES: monotone-integrated large-eddy simulation), and the type of initial interfacial and velocity perturbations for each simulation are also indicated.

the current DNS.

### B. Idealized initial conditions

While the specific details regarding the initial perturbation in many three-dimensional Rayleigh–Taylor simulations differ, a common theme unites most methodologies employed. Whether perturbations were imposed on the density field, mole fraction field, velocity field, or density interface (as noted in Table I) each simulation shared the common characteristic that the spectral content of the perturbations was not a function of coordinate direction. An early example of isotropic initial perturbations was reported by Youngs[1], where a random combination of Fourier modes in all directions was used to perturb the interface separating two fluids in a MILES.

Cook and Dimotakis[6] adopted a similar approach to Youngs, perturbing the mole fraction field instead of the initial interface. The perturbation field was generated as a two-dimensional field of random numbers (filtered to impose periodicity, transformed to **k**-space, and then Gaussian-filtered before transforming back to **x**-space). The filter was applied to fit the perturbations to a prescribed spectrum. The density field was isotropic and had broad-band perturbations in the homogeneous $xy$-plane. Three cases were considered with different perturbation spectra $E_\zeta(k)$, but with equal perturbation energy,

$$\int_0^{k_{\max}} \int_0^{k_{\max}} E_\zeta(k_x, k_y)\,\mathrm{d}k_x\,\mathrm{d}k_y \tag{1}$$

$$= \int_0^{2\pi} \int_0^{2\pi} \zeta(x,y)^2\,\frac{\mathrm{d}x\,\mathrm{d}y}{(2\pi)^2} = \int_0^{k_{\max}} E_\zeta(k)\,\mathrm{d}k\,.$$

Following a similar approach, Ristorcelli and Clark[10] perturbed the initial concentration field with a prescribed concentration spectrum, assuming a uniform distribution of phases. Other three-dimensional simulations have also adopted a similar process of imposing random perturbation, resulting in isotropic initial conditions.

### C. Approximations of simulation initial conditions using experiments

In the salt water/fresh water Rayleigh–Taylor mixing experiment of Linden and Redondo[19] the amount of mixed fluid was measured by a passive, equilibrium chemical reaction between the light and heavy fluids (mixing of acid and alkali). In the MILES[3] of this experiment, the removal of the barrier initially separating the fluids induced a long-wavelength two-dimensional perturbation, which was approximately modeled by the single-mode perturbation $\zeta(x) = a_0 \cos(2\pi x/\lambda)$, where $a_0 = 0.01H$ or $0.02H$ and $\lambda = H/6$ were chosen by visual comparisons with the experiment. No velocity perturbation was included. An additional perturbation was superimposed in order to break the two-dimensional symmetry of the modeled initial conditions,

$$\zeta(x,y) = \underbrace{\zeta(x)}_{\text{long wavelength}} + \underbrace{\mathrm{Re} \sum_{|m|,|n|=2}^{N/6} a_{mn}\,\mathrm{e}^{i(k_x x + k_y y)}}_{\text{random perturbation}}\,, \tag{2}$$

with $k_x = 2\pi m/H$ and $k_y = 2\pi n/H$ ($N$ is the number of grid points in each direction and $H$ is the height of the tank), so that the smallest wavelength was $\lambda_{\min} = 4\Delta x$ initially. The amplitudes $a_{mn}$ were scaled such that $\sqrt{\langle z_i^2 \rangle} = 0.02\lambda_{\min}$. The standard deviation of the random perturbation was $\sigma = 0.08\Delta x$. The barrier removal also generated small-scale turbulence modeled in some of the simulations by increasing the standard deviation.

A similar experiment was subsequently performed and simulated using MILES,[4] where discrepancies between previous experimental and numerical studies were attributed to an incomplete modeling of the initial conditions. For these simulations, an initial velocity perturbation was used to model the barrier removal. The initial streamfunction in the simulation was

$$\begin{aligned}\psi(x,0,z) \;&=\; U_{bar}\, L\, \frac{h_{bar}}{H} \qquad (3)\\ &\times \sum_{n=1}^{10} a_n \sin\left(\frac{n\pi x}{L}\right) \frac{\sinh\left[\frac{n\pi H}{2L}\left(1-2\frac{|z|}{H}\right)\right]}{\sinh\left(\frac{n\pi H}{2L}\right)},\end{aligned}$$

where $a_n$ are the fitted Fourier coefficients, $U_{bar}$ is the speed of removal of the barrier, and $L$ is the length of the tank. Both 'idealized' and 'real' initial conditions were used. The 'idealized' conditions had $\mathbf{v}(\mathbf{x},0)=\mathbf{0}$ and a random perturbation on the interface, consisting of a sum of Fourier modes with wavelengths in $[4\Delta x, 8\Delta x]$ and randomly chosen amplitudes having $\sigma = 0.08\Delta x$. The 'real' initial conditions included the velocity perturbation, where $v_x(x,0,z,t=0)=\partial\psi/\partial z$ and $v_z(x,0,z,t=0)=-\partial\psi/\partial x$ were generated by (3) and used the same random interfacial perturbations as in the ideal case. No attempt was made to match any measured spectrum of the initial experimental perturbations. Again, as was required in the MILES of Linden et al.[3], additional random perturbations were superimposed to break the initial symmetry of the modeled initial conditions. Note that the MILES[3,4] had *numerical* Schmidt numbers of $\mathcal{O}(1)$, while the salt water/fresh water experiments after which they were modeled had molecular Schmidt numbers of $\mathcal{O}(10^3)$.

To remove the necessity of superimposing additional perturbations that were not measured, three-dimensional MILES of Rayleigh–Taylor instability initialized directly with experimental velocity and density data measured in the water channel were performed.[16] The density perturbations were expressed in a form similar to Eq. (2). A similar interfacial perturbation was used in the comparative study of the predictions of different MILES codes applied to Rayleigh–Taylor instability growth[5] (where no velocity perturbations were used). The measured amplitudes of the 32 (or 16) longest modes obtained from the Fourier amplitudes of the thermocouple-measured density fluctuations at $x = 0.1$ cm downstream of the edge of the splitter plate were used for $a_{mn}$. To generate a two-dimensional perturbation in **k**-space, the Fourier amplitudes were multiplied by a two-dimensional random number field chosen to have a mean value of 1 and a standard deviation of $\sigma = 0.3$ in the azimuthal direction (*i.e.* it was assumed that the initial conditions are statistically-isotropic in the horizontal plane): this value of $\sigma$ ensured that the azimuthally-averaged spectra used in the simulations had the same energy for the included wavenumbers as in the experiment. The velocity perturbations were obtained from the gradient of the potential

$$\phi(\mathbf{x}) = \sum_{m=m_{\min}}^{m_{\max}} \sum_{n=n_{\min}}^{n_{\max}} \frac{a_{mn}}{k} \sin\left(k_m x\right) \sin\left(k_n y\right) \mathrm{e}^{-k|z|} \qquad (4)$$

with $k_m = 2\pi m/L_x$, $k_n = 2\pi n/L_y$, and $k=\sqrt{k_m^2+k_n^2}$. Particle-image velocimetry measurements at $x = 0.25$ cm were used to obtain the velocity data, and the $a_{mn}$ were chosen so that the integral of velocity spectra from the simulations and experiment agreed at this location. Again, these MILES had a *numerical* Schmidt number of $\mathcal{O}(1)$, while the experiments after which they were modeled had a molecular Schmidt number of 7.

## III. PARAMETERIZATION OF EXPERIMENTAL MEASUREMENTS FOR SIMULATION INITIAL CONDITIONS

A detailed discussion of the parameterization of the experimentally measured initial conditions and their current numerical implementation in the simulation code is presented here. For reference, a description of the water channel experiment from which the initial conditions have been measured is given first. The measured density and velocity perturbations are discussed, together with their conversion into perturbation spectra appropriate for use in the DNS. The relationship between the measured and parameterized spectra is also discussed, together with resolution issues, in the Appendix.

### A. Description of the water channel experiment

A complete description of the experimental facility, diagnostics, and measurements is available elsewhere,[17] and only a brief review is provided here. The water channel is an open-loop facility that creates an unstable stratification of hot and cold water. The temperature difference ($\Delta T \approx 5$ °C) induces the density difference by thermal expansion of the warmer fluid. Water from two 500 gallon tanks is pumped into the entrance plenum of the water channel. The two streams are initially separated by a thin splitter plate. At the termination of the splitter plate, an unstable stratification of the colder fluid over the warmer fluid is generated and a statistically-stationary Rayleigh–Taylor instability-driven mixing layer forms downstream.[20–24] The downstream distance from the splitter plate $x$ is related to the time of instability development by Taylor's hypothesis[25,26]

$$x = \overline{u}_x\, t\,, \qquad (5)$$

where $\overline{u}_x \approx 4.75$ cm/s is the mean velocity of each stream entering the water channel.

### B. Density perturbation

The initial density field in the DNS is modeled as

$$\rho(\mathbf{x},t=0)=\frac{\rho_1+\rho_2}{2}+\frac{\rho_1-\rho_2}{2}\,\mathrm{erf}\left[\frac{z+\zeta(x,y)}{\varepsilon}\right], \quad (6)$$

where $\rho_1>\rho_2$, $\zeta(x,y)$ is the two-dimensional initial interfacial perturbation, $\varepsilon=0.15$ cm is the half-width of the initially-diffuse interface separating the heavier and lighter fluid, and $\mathrm{erf}(\cdot)$ is the error function. The initial interfacial perturbation $\zeta(x,y)$ is defined as the local vertical displacement of the point at which $\rho=(\rho_1+\rho_2)/2$ from the centerplane ($z=0$) and has the same units as $z$ and $\varepsilon$.

Perturbations to the density field in the $x$-direction were measured in the water channel using a high-resolution thermocouple placed on the centerplane ($z=0$) a distance $x=0.5$ cm downstream from the trailing edge of the splitter plate (see Ref. 17). Temperature measurements were converted to density using the equation of state of water. The density variance spectrum

$$E_\rho(k_x)=\frac{|\widehat{\rho}(k_x)|^2}{4\,\Delta k_x} \quad (7)$$

was then calculated from the Fourier amplitudes of the density fluctuations

$$\widehat{\rho}(k_x)=\frac{2}{L_x}\int_0^{L_x}\rho(x)'\,\mathrm{e}^{-ik_x x}\,\mathrm{d}x\,, \quad (8)$$

where $\rho(x)'$ is the measured density fluctuation (obtained by subtracting the mean density from the pointwise values of the measured full density field), $L_x=\overline{u}_x t$ is the length of the domain in the streamwise $x$-direction given by Taylor's hypothesis (5), and $\Delta k_x$ is the spacing between wave number bins. It follows from Eq. (7) that the density perturbation amplitude is $|\widehat{\rho}(k_x)|=\sqrt{4E_\rho(k_x)\Delta k_x}$.

Interfacial perturbations were also measured in the spanwise $y$-direction using planar laser-induced fluorescence (see Ref. 17). By seeding the top stream with a fluorescing dye and aligning a laser sheet along the trailing edge of the splitter plate, the interface $\zeta(y)$ between the hot and cold fluids was detected. The modal amplitudes and interfacial perturbation variance spectrum were determined using Eqs. (7) and (8).

Interfacial perturbation spectra from the experiment in the $x$- and $y$-directions, $\widehat{\zeta}(k_x)$ and $\widehat{\zeta}(k_y)$ respectively, were used to formulate

$$\zeta(x,y)=\sum_{k_x=k_{\min}}^{k_{\max}}\widehat{\zeta}(k_x)\,\mathrm{e}^{ik_x x}+\sum_{k_y=k_{\min}}^{k_{\max}}\widehat{\zeta}(k_y)\,\mathrm{e}^{ik_y y} \quad (9)$$

in the DNS, where $k_x=2\pi/\lambda_x$ and $k_y=2\pi/\lambda_y$ are the wave numbers in the $x$- and $y$-directions. The perturbation amplitudes, $\left|\widehat{\zeta}(k_x)\right|$ and $\left|\widehat{\zeta}(k_y)\right|$, were taken from the experimentally-measured spectra shown in Fig. 1:

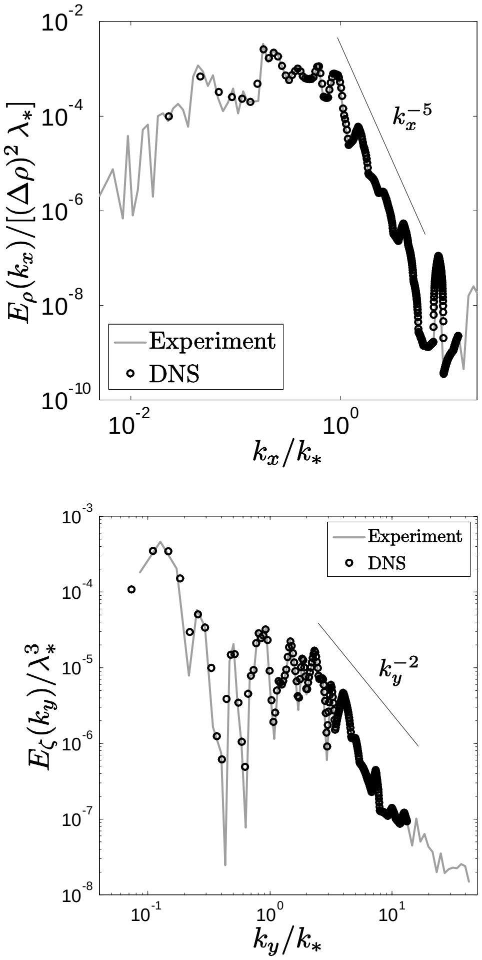

FIG. 1: The normalized initial density perturbation spectrum in the $x$-direction (top) and the normalized initial interfacial perturbation spectrum in the $y$-direction (bottom) at the centerplane of the mixing layer.

$$\left|\widehat{\zeta}(k_i)\right|=\sqrt{4E_\zeta(k_i)\,\Delta k_{\,i}} \quad (10)$$

($i=x,y$), where $E_\zeta(k_x)$ is determined from the measured $E_\rho(k_x)$ spectrum by relating density perturbations to interfacial perturbations (see the Appendix for details). Phases for each mode were chosen from a uniform distribution of Gaussian random values in $[-\pi,\pi]$. The initial conditions spectra shown in Figs. 1 and 2 are normalized using the most unstable wavelength $\lambda_*=0.661$ cm and the corresponding most unstable wavenumber $k_*=9.51$ cm$^{-1}$.

### C. Velocity perturbation

The initial velocity fluctuations present in the mixing layer at the onset of the instability were measured using

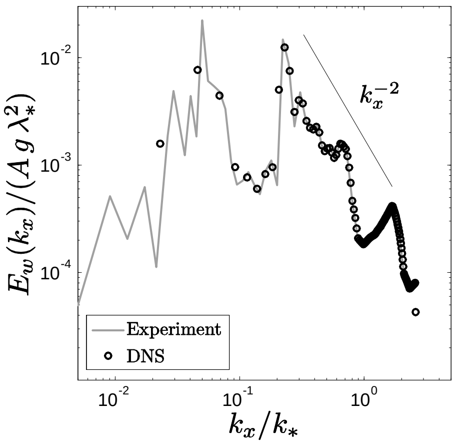

FIG. 2: The normalized initial vertical velocity perturbation spectrum in the $x$-direction at the centerplane of the mixing layer.

particle-image velocimetry (see Ref. 17). An initial velocity field based on the measured initial vertical velocity variance spectrum at the centerplane ($z = 0$), shown in Fig. 2, was then constructed. To apply the initial centerplane vertical velocity fluctuations to the entire computational domain, a velocity field based on $E_w(k_x)$ must be parameterized. This is accomplished by defining a velocity potential field

$$\phi(\mathbf{x}, t=0) = \sum_{k_x=k_{\min}}^{k_{\max}} \frac{\widehat{w}(k_x)}{k_x} \begin{cases} \mathrm{e}^{ik_x x - k_x z} & \text{if } z \geq 0 \\ \mathrm{e}^{ik_x x + k_x z} & \text{if } z < 0 \end{cases} \quad (11)$$

similar to that used in the linear (small-amplitude) analysis of Kelvin–Helmholtz and Rayleigh–Taylor instabilities.[27] Then the initial velocity field is the sum of the gradient of the potential (the irrotational component) and a term proportional to the density gradient (a diffusion velocity)

$$u_i(\mathbf{x}, t=0) = \left.\frac{\partial \phi}{\partial x_i}\right|_{t=0} - \frac{D}{\rho}\left.\frac{\partial \rho}{\partial x_i}\right|_{t=0} ; \quad i = x, y, z\,, \quad (12)$$

where $D = \nu/Sc$ is the mass diffusivity, $\nu$ is the kinematic viscosity, and $Sc = 7$ is the Schmidt number (see Table II). The density gradient term in Eq. (12) accounts for the velocity field that exists due to the initial density gradient between the top and bottom fluids, as $\boldsymbol{\nabla} \cdot \mathbf{u} \neq 0$ when $D\boldsymbol{\nabla}\rho \neq 0$.[28,29] The maximum velocity imposed by the initial perturbation is 0.327 cm/s [first term on the right side of Eq. (12)], and the second term on the right side of Eq. (12) has a maximum value $\sim 1.0 \times 10^{-5}$ cm/s. The initial vorticity field consists of a vortex sheet aligned in the $y$-direction and varying in $x$ only on the $z = 0$ plane, and a density gradient contribution. Note that fiducials showing a $k_y^{-2}$ and $k_x^{-2}$ spectrum are shown in Figs. 1 and 2, respectively, for $E_\zeta(k_y)$ and $E_w(k_x)$. For reference, simulations with initial perturbations satisfying a $k^{-2}$ power law were performed by Dimonte *et al.*[5] and the deuterium-tritium ice surface roughness in inertial confinement fusion target capsules has a similar approximate power-law.[30]

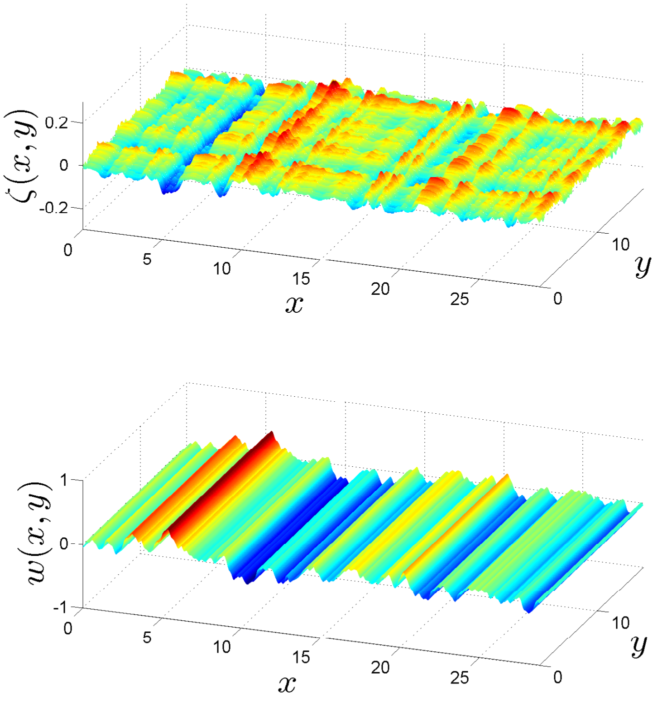

FIG. 3: (Color online) Initial interfacial (top) and centerplane ($z = 0$) vertical velocity (bottom) perturbation isosurfaces in the DNS. Red represents large values and blue represents small values.

A visualization of the anisotropic initial interfacial and vertical velocity perturbations on the centerplane is shown in Fig. 3. There are no velocity perturbations in the $y$-direction. Thus, any three-dimensional structures that develop within the turbulent mixing layer are due to the interfacial perturbations in the $y$-direction. Note the two-dimensional ‘roll’ structure in the initial velocity perturbations, which (by construction) are also qualitatively observed at very early times in the experiment (see Fig. 6).

## IV. NUMERICAL METHOD

The parameterized initial interfacial and velocity perturbations described in Sec. III were used in a DNS approximating the conditions of the water channel experiment. The variable-density fluid equations solved, simulation parameters, simulation geometry, and boundary conditions are described here.

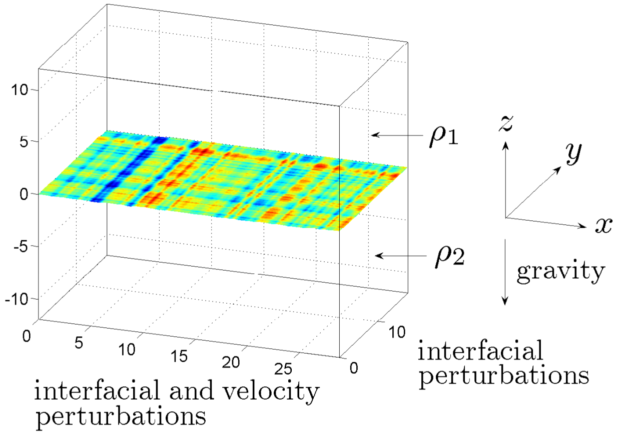
10
5
0
-5
-10
0
5
10
15
20
25
10
0
$\rho_1$
$\rho_2$
$z$
$y$
$x$
gravity
interfacial perturbations
interfacial and velocity perturbations

FIG. 4: (Color online) Schematic of the computational domain for the DNS showing the geometry and direction of gravity. The isosurface of the initial interfacial perturbation $\zeta(x, y)$ is shown on the centerplane ($z = 0$). In the experiment, the inflow is at $x = 0$, so that the $x$-, $y$-, and $z$-directions correspond to the streamwise, spanwise, and cross-stream directions, respectively. The coordinate directions in which experimental measurements were used are also indicated.

### A. Equations describing variable-density Rayleigh–Taylor flow

The variable-density incompressible density and momentum equations are[6]

$$\frac{\partial \rho}{\partial t} + \frac{\partial}{\partial x_j}(\rho\, u_j) = 0\,, \tag{13}$$

$$\frac{\partial}{\partial t}(\rho\, u_i) + \frac{\partial}{\partial x_j}(\rho\, u_i\, u_j) = \rho\, g_i - \frac{\partial p}{\partial x_i} + \frac{\partial \sigma_{ij}}{\partial x_j}\,, \tag{14}$$

where $\rho$ is the density, $u_i$ is the velocity field, $g_i = (0, 0, -g)$ is the gravitational field, $p$ is the pressure, and $\sigma_{ij} = \mu\left(\partial u_i/\partial x_j + \partial u_j/\partial x_i - \frac{2}{3}\delta_{ij}\partial u_k/\partial x_k\right)$ is the viscous stress tensor with dynamic viscosity $\mu = \rho\nu$ and kinematic viscosity $\nu = (\mu_1 + \mu_2)/(\rho_1 + \rho_2)$. The velocity divergence in $\sigma_{ij}$ is retained as the flow is not solenoidal due to molecular mass diffusion ($D \neq 0$).[28,29] However, $\boldsymbol{\nabla} \cdot \mathbf{u}$ is small for the small Atwood number flow considered here.

In the water channel experiment,[17] a small temperature difference was used to induce a density difference between two superposed water streams. The temperature equation is not solved in the DNS; instead, the heavy fluid mass fraction equation in the Fickian diffusion approximation

$$\frac{\partial}{\partial t}(\rho\, m_1) + \frac{\partial}{\partial x_j}(\rho\, m_1\, u_j) = \frac{\partial}{\partial x_j}\left(\rho\, D\, \frac{\partial m_1}{\partial x_j}\right) \tag{15}$$

is solved, where $m_r$ is the mass fraction of fluid $r = 1, 2$, $m_1 + m_2 = 1$, and $D$ is the mass diffusivity of both fluids. In the Fickian approximation, the analogy between temperature and mass fraction is mathematically equivalent under the assumption of equal species diffusivities. Thus, $D$ was equated to the thermal diffusivity of water in order to simulate the experiment ($Pr \equiv Sc = 7$).

### B. Numerical methods and boundary conditions

A spectral/compact difference scheme was used to solve Eqs. (13)–(15). The code was modified to use the parameterized initial conditions discussed in Sec. III. As the DNS does not use inflow and outflow boundary conditions to represent the water streams entering and exiting the channel at a constant velocity, Taylor's hypothesis [Eq. (5)] is used to relate the instability development downstream in the channel to the time-evolution in the DNS, *i.e.* the numerical simulation is performed in a reference frame moving with the mean flow velocity in the $x$-direction (as in simulations of shear layers[31]). Periodic boundary conditions were imposed in the $x$- and $y$-directions (orthogonal to gravity), allowing a spectral discretization with uniform grid spacing in these directions.[32] In the $z$-direction (parallel to gravity), free-slip boundary conditions were imposed at the top and bottom of the domain, and a tenth-order compact scheme was used for the spatial discretization.[33] As a result of the difference in resolving power of the spectral and compact difference schemes, the grid resolution in the vertical direction was set to $\Delta z = 0.75\Delta x$. Further details on resolution considerations and the implementation of the boundary conditions can be found elsewhere.[6,13]

A third-order Adams–Bashforth–Moulton predictor–corrector scheme was used to advance Eqs. (13)–(15) in time. This two-step predictor–corrector scheme was further decomposed in order to advance the momentum equation, where an incompressible pressure-projection scheme separated the advection/diffusion and acceleration/body force updates. First, the momentum field without pressure gradient and body force was estimated at time step $n + 1$. Next, a pressure Poisson equation was solved to ensure mass conservation. The pressure gradient and body force were then included to estimate the momentum at time step $n + 1$, denoted $(\rho u_i)^*$. Applying the corrector step to $(\rho u_i)^*$ yields a final value of the momentum $(\rho u_i)^{n+1}$.

### C. Simulation parameters and geometry

The physical parameters in the DNS were chosen to match a typical water channel experiment as closely as possible, and are given in Table II. The water channel has cross-sectional dimensions of 20 cm deep and 32 cm high (direction of gravity). With a typical mean advective velocity $\overline{u}_x \approx 4.75$ cm/s and data capture times from 1–10 minutes in duration, the longest resolvable wavelengths in the streamwise direction are $\gtrsim 190$ cm. However, a computational domain size of 190 cm $\times 20$ cm

| Parameter | Value |
|---|---|
| $\rho_1$ | 0.9985986 g/cm$^3$ |
| $\rho_2$ | 0.9970479 g/cm$^3$ |
| $A$ | $7.5 \times 10^{-4}$ |
| $g$ | 981 cm/s$^2$ |
| $\mu_1$ | 0.009 g/(cm s) |
| $\mu_2$ | 0.011 g/(cm s) |
| $Sc \equiv Pr$ | 7 |

TABLE II: Physical parameters used in the DNS of the water channel experiment.

$\times$ 32 cm is not feasible due to resolution requirements and computational resource limitations: at the grid resolution used in the present study, this would require a grid consisting of $N_x \times N_y \times N_z = 7600 \times 800 \times 1707$ points (in actuality, the required grid size would be even larger, as smaller grid spacings are needed to resolve the flow field that would achieve larger Reynolds numbers than in the present study). Thus, an acceptable domain size must be chosen such that resolution considerations could be met while also incorporating longer wavelengths present in the experiment that may influence the mixing layer dynamics.[3,34] The chosen computational domain size was $L_x \times L_y \times L_z = 28.8$ cm $\times\, 18$ cm $\times\, 24$ cm, representing an interior portion of the full channel with dimensions $L_x \times L_y \times L_z = 190$ cm $\times\, 20$ cm $\times\, 32$ cm (see Fig. 4), and the grid size was $N_x \times N_y \times N_z = 1152 \times 760 \times 1280 = 1,120,665,600$ points. To our knowledge, this is the second largest reported DNS of Rayleigh–Taylor mixing performed to date after the simulation of Cabot and Cook,[8] which achieved a final grid size of $3072^3$.

The estimated Kolmogorov scale $\eta_K \approx h Re_h^{-3/4} \approx 0.055$ cm gives a lower bound resolution limit velocity field near the end of the simulation, where the mixing layer width is $h \approx 15$ cm and the Reynolds number based on $h$ is $Re_h \approx 1700$. Here, the integral scale Reynolds number is[16]

$$Re_h(t) = \frac{0.35\sqrt{g\,A\,h^3}}{\nu}\;, \tag{16}$$

the evolution of which is discussed further in Sec. II A of Part II As $Sc > 1$, the resolution requirements for the scalar (density) field are even more stringent, where the smallest density fluctuations are given by the Batchelor scale $\eta_B = \eta_K Sc^{-1/2} \approx 0.021$ cm. The DNS has $\Delta x = \Delta y = 0.025$ cm and $\Delta z = 0.01875$ cm, so that the flow is slightly under-resolved and aliasing errors are generated as the Reynolds number increases. Such aliasing errors (predominantly in the density field) were filtered out using a sharp spectral low-pass filter at mode number $k_x = k_y = 113.8$ cm$^{-1}$, or approximately at twice the grid spacing. While this filtering effectively removed the aliasing errors, a small fraction of energy (having negligible effect on the mixing dynamics) was also removed from the largest wave numbers. Additional details on the filtering methods can be found elsewhere.[13] The simulation was run to a final time when the mixing layer reached $h(t) = 0.62 L_z$. Beyond this time, the upper and lower boundaries began to influence the mixing layer growth through nonlocal pressure effects, which in turn influenced velocity fluctuations outside the mixing layer.

### D. Computational details

The simulations were performed using a parallel `Fortran 90` code on the Zeus computer at the Lawrence Livermore National Laboratory; 48 nodes (384 processors) were used. Each node had eight 2.4 GHz AMD dual-core Socket F Opteron® processors and 16 Gb of memory. A total of 74 restart dumps were generated for data analysis, totaling 6.29 Tb of data. All fields were stored in double precision format.

## V. COMPARISONS OF QUANTITIES FROM THE DIRECT NUMERICAL SIMULATION WITH EXPERIMENTAL MEASUREMENTS

The DNS model of the water channel experiment is validated here by comparing simulation results with available experimental measurements. Qualitative comparisons between the experiment and the simulated mixing layer exhibit good agreement. Measurements of the mixing layer growth parameter $\alpha_b$, fluctuating velocity statistics, and mixing statistics also exhibit favorable agreement.

### A. Statistical averaging

Statistical analysis of Rayleigh–Taylor mixing requires averaging over an ensemble of realizations. Due to the extreme computational requirements of DNS, it is generally impractical to perform an ensemble of well-resolved simulations for averaging purposes. However, the simple flow geometry assumed in the current simulation model implies statistical homogeneity in the $x$- and $y$-directions (orthogonal to the direction of gravity). Thus, ensemble averages are defined as the average over $xy$-planes,[2,10] so that the Reynolds average (denoted by an overbar) of a field $\phi(\mathbf{x}, t)$ is

$$\overline{\phi}(z,t) = \frac{1}{L_x\,L_y}\int_0^{L_x}\int_0^{L_y}\phi(\mathbf{x},t)\,\mathrm{d}y\,\mathrm{d}x\,. \tag{17}$$

The instantaneous values of a given field can be decomposed into mean and fluctuating (denoted by a prime) components according to $\phi(\mathbf{x},t) = \overline{\phi}(z,t) + \phi(\mathbf{x},t)'$. As a consequence of this averaging, the fluctuation of a field averages to zero in a given plane, $\overline{\phi'} = 0$.

### B. Qualitative observations and comparisons

To facilitate comparisons between the DNS and the experiment, time is normalized by

$$\tau = \sqrt{\frac{g\,A}{H}}\,t\,, \tag{18}$$

where $A \equiv (\rho_1 - \rho_2)/(\rho_1 + \rho_2) = 7.5 \times 10^{-4}$ is the Atwood number, $g$ is the acceleration, and $H = 32$ cm is the vertical height of the water channel (n.b., $H$ is not equal to the height of the computational domain $L_z$). This dimensionless time has been adopted in order to compare the DNS results with the experiment [the characteristic timescale is $\sqrt{H/(gA)} = 6.59$ s]; however, other time scales may be used instead. For example, the most unstable wavelength according to linear stability analysis[35] $\lambda_* \approx 4\pi\left[\nu^2/(gA)\right]^{1/3} = 0.66$ cm can be used to normalize time according to[13,36] $\tau_\lambda = \sqrt{gA/\lambda_*}t$. Another time scale normalized by the growth rate of the most unstable wavelength $\omega_{max} = \sqrt{2\pi gA/\lambda_*} = 2.65$ s$^{-1}$ can be used. Results are then characterized in terms of the number of $e$-folding periods $\tau_e = \omega_{max}t$. This scaling becomes advantageous when studying transitional flows where, for example, approximately nine $e$-folding periods are required for temporal instabilities to transition to turbulence in a boundary layer.[37,38] The relationship between these alternate time scalings and (18) are given by $\tau_\lambda/\tau = 6.96$ and $\tau_e/\tau = 11.47$ (n.b., $\tau_\lambda$ and $\tau_e$ differ only by a factor of $\sqrt{2\pi}$). Accordingly, the DNS reaches a dimensionless time $\tau = 1.52$ or $\tau_\lambda = 10.58$ and $\tau_e = 17.4$. Thus, it may be possible to classify the final stages of the DNS as 'turbulent' according to the $e$-folding criterion above. A more detailed discussion of the transitional and turbulent regimes observed in the DNS is given in Part II.

Experimental observations from the water channel experiment indicate that the initial velocity perturbations dominate the early-time growth of the mixing.[17] This was also observed in the DNS, where the initial growth of the mixing layer was primarily two-dimensional. In simulations with isotropic initial conditions, the initial structures that develop from the unstable configuration are approximately spherical in shape.[39] Each rising and falling structure approximately obeys single-mode dynamics until secondary instabilities develop and nonlinear dynamics begin to dominate the mixing layer.[40,41] This is not the case here, where the initial growth of the mixing layer better resembles the early-time growth in two-dimensional simulations.[14] This is clearly seen in the early-time evolution of the $f_1 = 0.5$ isosurface shown in Fig. 5. Such growth is also observed in the water channel experiments, where little spanwise structure or variation is observed during the early-time development of the mixing layer.

At the onset of the instability, the initial velocity field forms a vortex sheet with variations only in the $x$-direction. As a result, little structure exists in the spanwise or $y$-direction. This is shown in Fig. 7, where at early times ($\tau = 0.1$ and 0.43) the vorticity variance in the $x$-direction ($\overline{\omega_1'^2}$) is small with respect to that in the $y$-direction ($\overline{\omega_2'^2}$); the overbar denotes an average in the two periodic directions and $\omega_i' = \omega_i - \overline{\omega}_i$. Spanwise structure slowly develops as baroclinic production of vorticity in the $y$-direction results from the growth of the $\widehat{\zeta}(k_y)$ perturbations [see Eq. (A.3)]. As the interpenetration rate of the initial structures grows in magnitude, the material surface area on the rising bubble and falling spikes is stretched. As a result, this stretches the vortex lines in the $x$-direction, increasing their strength and creating 'rib-like' structures along the cylindrical structures. Such rib-like structures are evident by $\tau = 0.5$, as seen in Fig. 5. This nonlinear transition to a more three-dimensional mixing layer can also be seen in the difference between the early- and late-time vorticity variance profiles in Fig. 7. By $\tau > 1$, the vorticity fluctuations in the $x$- and $y$-directions are approximately equal.

At $\tau \approx 1$, the mixing layer exhibits a more three-dimensional flow structure as shown by the $f_1 = 0.5$ isosurface in Fig. 5. This nonlinear transition to a more complex internal structure is also observed in water channel experiment at $\tau \approx 1$. This transition is more easily visualized in the DNS, where the nonlinear interactions of the stretched vortex lines contort the interface in the direction not aligned with the $x$- and $y$-axes, as seen by $\tau = 1.01$. During this nonlinear transition, individual vortex lines are broken to form vortex rings, thereby creating more three-dimensional bubbles and spikes. The bubbles and spikes appear to be closer to spherical in morphology than cylindrical by this time.

The isosurfaces of the density field can be qualitatively compared with the water channel experiment. An image of the initial development of the mixing layer in a typical experiment is shown in Fig. 6. The initial, two-dimensional disturbance generated by the splitter plate is evident on the left-hand side, which is similar to the initial development observed in the DNS. As the Rayleigh–Taylor mixing layer grows, so do the perturbations in the spanwise direction in both the DNS and in the experiment. As the mixing layer continues to grow, ripples along the top edges of the rising structures break into individual bubbles, and more three-dimensional structure is evident at later times. This mechanism is seen in both the water channel on the right-hand side of Fig. 6, and in the DNS in Fig. 5.

### C. Mixing layer growth

The total width of the mixing layer is typically determined by the distance between the penetration of the bubble and spike fronts into each respective fluid.[20,42] Consistent with the experiment, the bubble and spike front penetrations are defined here by the $\overline{f}_1(z,t) = 0.95$

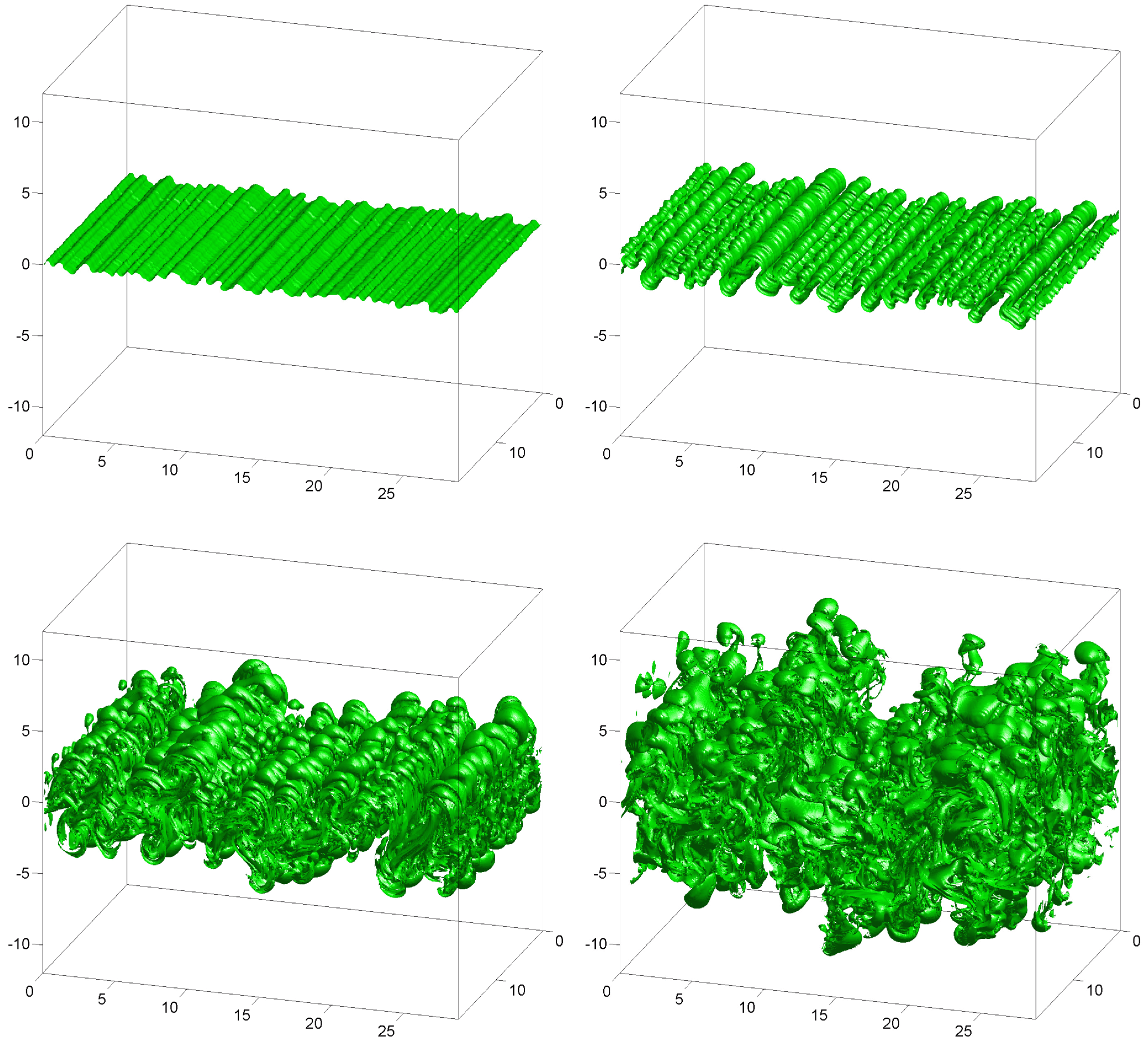

FIG. 5: (Color online) The $f_1 = 0.5$ volume fraction isosurface at $\tau = 0.21$ (top left), $\tau = 0.50$ (top right), $\tau = 1.01$ (bottom left), and $\tau = 1.52$ (bottom right) from the DNS.

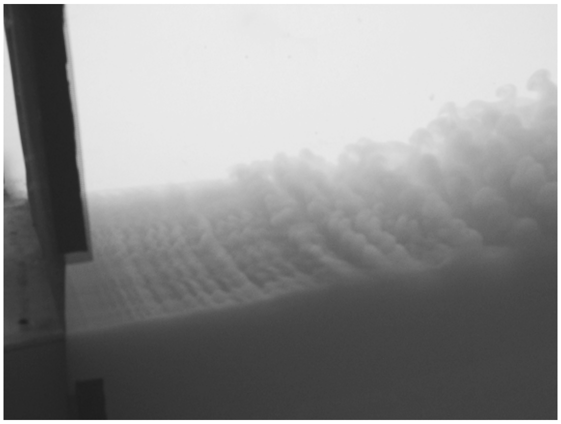

FIG. 6: Photograph of the initial development of a Rayleigh–Taylor mixing layer in the water channel, where a small amount of milk has been added to the bottom stream for visualization purposes. The flow is from left-to-right.

and $\overline{f}_1(z,t) = 0.05$ thresholds, respectively, where

$$\overline{f}_1(z,t) = \frac{\overline{\rho}(z,t) - \rho_2}{\rho_1 - \rho_2} \tag{19}$$

is the mean volume fraction of fluid 1 at a given vertical location $z$. A first-order validation of the DNS is given by a comparison of the mixing layer growth and its late time growth rate. A comparison of the bubble and spike front widths, $h_b$ and $h_s$, from the DNS and the water channel experiment[21] (based on the 5–95% mean volume fraction thresholds) is shown in Fig. 8. The bubble and spike penetrations are slightly underestimated by the DNS.

In the turbulent regime, nonlinear extensions of classical linear instability theory,[41] dimensional analysis,[43] bubble merger (or competition) models,[34,44,45] and direct numerical simulations[6,8] show that the mixing layer width (when dissipative, diffusive, surface tension, and other scale-similarity breaking effects can be neglected)

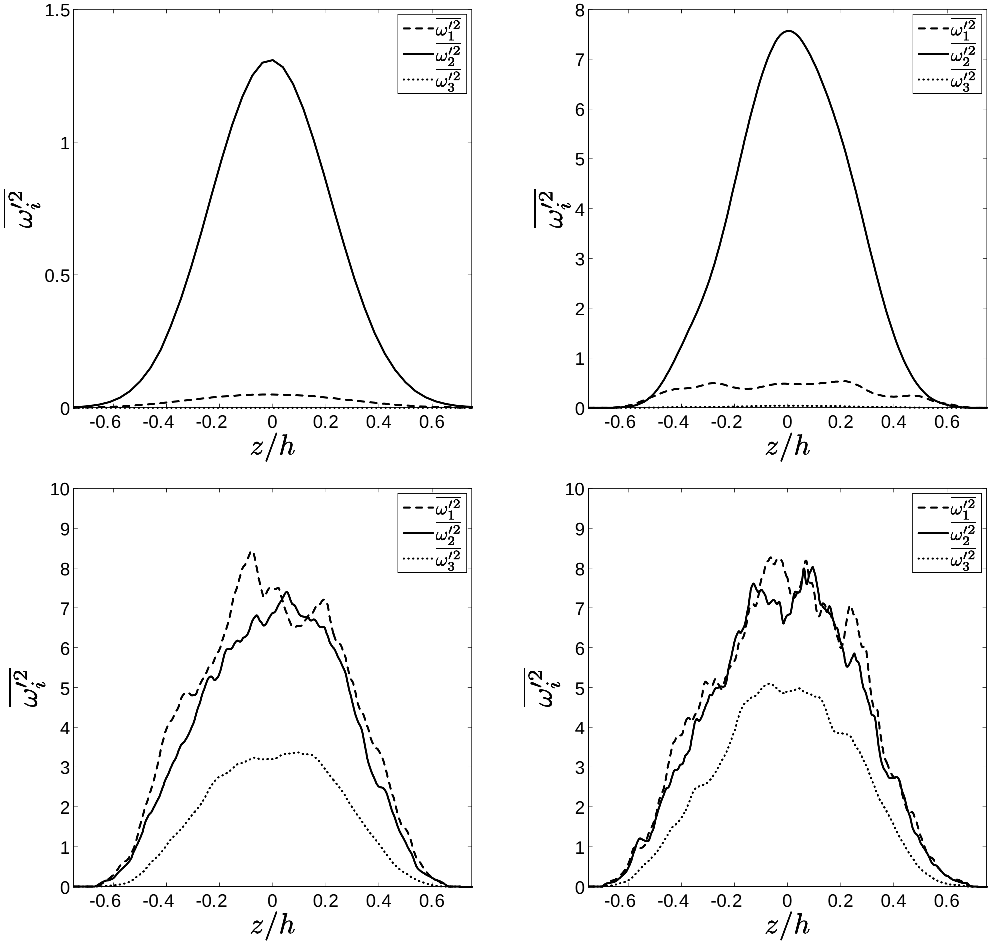

FIG. 7: Profiles of the vorticity variance (in units of $\mathrm{s}^{-1}$) in each coordinate direction from the DNS at integral-scale Reynolds numbers $Re_h \approx 10$, 100, 1000, and 1710, corresponding to dimensionless times $\tau = 0.10$, 0.43, 1.16, and 1.52.

scales as

$$h(t) = h_b(t) - h_s(t) = \alpha\, A\, g\, t^2\,, \tag{20}$$

in the late-time self-similar regime, where $\alpha$ is dimensionless. As $h_b \approx |h_s| \approx h/2$ at small Atwood numbers, the self-similar growth parameter $\alpha_b \approx \alpha/2$ can be determined from

$$\frac{h}{2} \approx h_b = \alpha_b\, A\, g\, t^2\,. \tag{21}$$

Equation (21) is recovered for the late-time growth of a small Atwood number mixing layer by self-similar analysis[10,41] or dimensional analysis.[6] A more general expression for the self-similar growth is given by the solution of the ordinary differential equation[10]

$$\left(\frac{\mathrm{d}h_b}{\mathrm{d}t}\right)^2 = 4\,\alpha_b\, A\, g\, h_b \tag{22}$$

obtained from a self-similar analysis of the second-moment equations. Solving Eq. (22) shows that $h_b$ is proportional to a sum of terms that scale as $t^n$ with $n = 0, 1$, and 2.

While various methods for determining a late-time value of $\alpha_b$ are possible, three independent measurements are examined here. First, from Eq. (21), the late-time slope of $h/2$ plotted against $Agt^2$ is considered. While this method is robust, it is not free from the influence of the $t^1$ and $t^0$ terms. The second method directly computes a time-dependent, effective $\alpha_b$ from the time derivative of Eq. (21) (which implicitly assumes that $\alpha_b$ is either a constant or varies very slowly),

$$\alpha_b(t) = \frac{1}{4\, A\, g\, t}\,\frac{\mathrm{d}h}{\mathrm{d}t}\,, \tag{23}$$

which eliminates the $t^1$ dependence of (21) and reduces the $t^0$ dependence. Finally, a time-dependent, effective $\alpha_b$ is directly calculated from Eq. (22). The various measures of $\alpha_b$ are shown in Fig. 9. The DNS reached a dimensionless time $\tau = 1.52$, which should be sufficiently late to realize self-similar growth as measured in the water channel. Self-similar scaling of the mixing layer width (*i.e.* quadratic growth) was observed for $\tau \gtrsim 1.2$

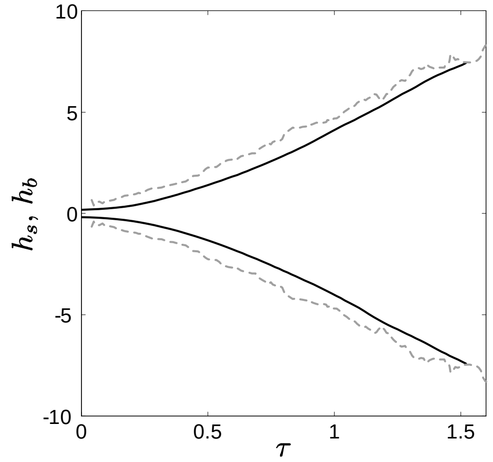

FIG. 8: Evolution of the bubble and spike front widths, $h_b$ and $h_s$ (cm), from the DNS (solid lines) and the water channel experiment (dashed lines).

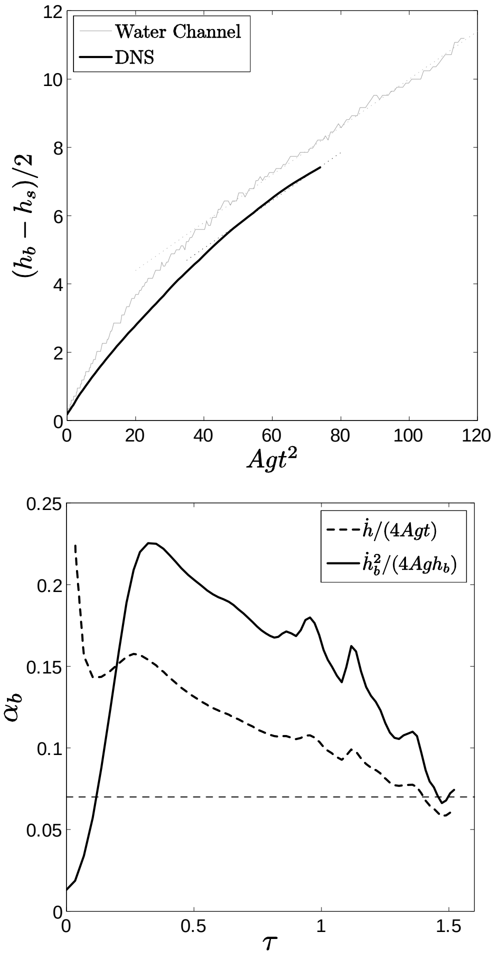

FIG. 9: Evolution of the mixing layer growth parameter $\alpha_b$ from the DNS using the mixing layer half-width (top) and from Eqs. (23) and (22) (bottom). A fiducial denoting $\alpha_b = 0.07$ is shown in the bottom figure.

in previous water channel experiments.[20] The growth parameter $\alpha_b$ inferred from the DNS appears to approach the experimental value $\alpha_b \approx 0.07$ for $\tau > 1.3$; however, it is difficult to conclude that $\alpha_b = 0.07$ is the asymptotic value in the DNS due to the domain size constraints. The experiments of Linden et al.[3] gave $\alpha_b = 0.044 \pm 0.005$ and the simulation of this experiment gave $\alpha_b \approx 0.035$. The simulations of Dalziel et al.[4] did not provide an unambiguous estimate of $\alpha_b$. The MILES of Ramaprabhu and Andrews[16] gave $\alpha_b \approx 0.06$ in reasonably good agreement with their experimentally-measured value $\alpha_b \approx 0.075$.

### D. Statistical convergence

Before a comparison of second-order velocity and density statistics is presented, an estimate of the relative uncertainty in the statistics is required. The statistical uncertainty (95% confidence interval bounds) in the averaged statistics may be quantified by $w_\phi = \pm 1.96\sqrt{s_\phi^2/N_\phi}$, where $s_\phi^2$ is the sample variance of the statistic $\phi$ and $N_\phi$ is the number of samples (*i.e.* turbulent structures) over which the average was taken.[46] Accordingly, the statistical uncertainty in a given mean is proportional to $1/\sqrt{N_\phi}$. Thus, as the DNS evolves in time and the turbulent length scales grow, fewer structures are available to calculate a mean value.

The dominant wavelength corresponding to a fluctuating scalar field $\phi(x,t)'$ based on the energy content of its spectrum $E_\phi(k,z,t)$ is[47] $\lambda_\phi(z,t) = 2\pi \int_{k_{\min}}^{k_{\max}} k^{-1} E_\phi(k,z,t)\mathrm{d}k \left[\int_{k_{\min}}^{k_{\max}} E_\phi(k,z,t)\mathrm{d}k\right]^{-1}$, where the factor of $2\pi$ results from defining wave numbers as $k = 2\pi/\lambda$. Due to the anisotropy of the implemented initial conditions, the turbulent scales of motion and statistics are not generally equal in all directions. Accordingly, the dominant wavelength in each coordinate direction

$$\lambda_{\phi,i}(z,t) = 2\pi \, \frac{\int_{k_{i,\min}}^{k_{i,\max}} \frac{E_\phi(k_i,z,t)}{k_i} \, \mathrm{d}k_i}{\int_{k_{i,\min}}^{k_{i,\max}} E_\phi(k_i,z,t) \, \mathrm{d}k_i} \tag{24}$$

($i = x, y$) is examined separately. The evolution of the dominant wavelengths for all three velocity components and the density at the centerplane of the mixing layer is shown in Fig. 10. As the Reynolds number increases, the dominant energy-containing scales also increase in size. In general, the velocity and density fields yield similar dominant wavelengths. However, due to the sustained anisotropy resulting from the initial conditions, the dominant wavelengths in the $x$- and $y$-directions remain distinct out to the final time $\tau = 1.52$.

The total number of turbulent structures within the domain is defined here as the product

$$N_\phi = \left(\frac{2\,L_x}{\lambda_{\phi,x}}\right)\left(\frac{2\,L_y}{\lambda_{\phi,y}}\right), \tag{25}$$

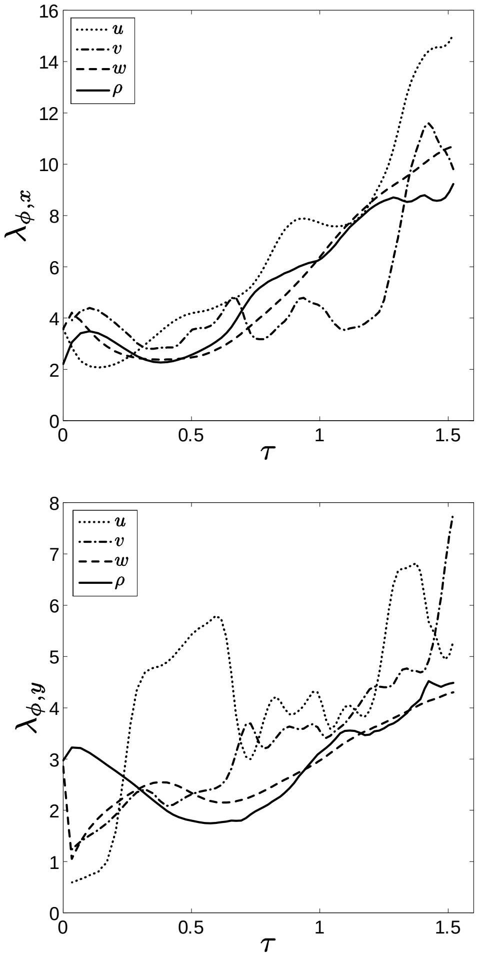

FIG. 10: Evolution of dominant wavelengths in the $x$-direction (top) and the $y$-direction (bottom) (both in cm) on the centerplane ($z = 0$) of the mixing layer based on each velocity component and density from the DNS.

where two structures (one bubble and one spike) are taken per wavelength. As the Reynolds number increases, the total number of dominant, energy-containing structures included in an ensemble average decreases. The total number of turbulent structures, based on the vertical velocity and density fields is shown in Fig. 11 as a function of the Reynolds number [Eq. (16)]. As expected in a flow with rising and falling buoyant structures, the strong correlation between vertical velocity and density fluctuations results in $N_\rho \approx N_w$. The uncertainty in all statistics presented scales as $1/\sqrt{N_\phi}$, and thus, oscillations in averaged quantities grow at late-time as there are only $N_\phi \approx 50$ structures at the final dimensionless time $\tau = 1.52$. Beyond the transitional stage of the mixing layer growth, $N_\phi \sim Re_h^{-1}$.

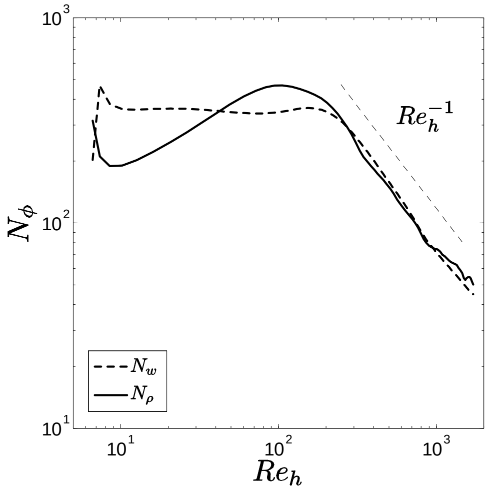

FIG. 11: Number of turbulent structures on the centerplane ($z = 0$) of the mixing layer, $N_w$ and $N_\rho$, based on the dominant wavelengths $\lambda_w$ and $\lambda_\rho$ as a function of integral-scale Reynolds number from the DNS. A fiducial corresponding to $Re_h^{-1}$ is also shown.

### E. Velocity variances

In addition to comparing integral-scale (*i.e.* large-scale) statistics between the DNS and the experiment, the evolution of the velocity variances on the centerplane of the mixing layer are also compared. The centerplane velocity variances shown in Fig. 12 agree well with the experiment up to $\tau \approx 0.5$. Beyond $\tau = 0.5$, the DNS yields lower values of $\overline{w'^2}$ than measured in the experiment. This is likely attributable to the finite computational domain size, which limits the spectral dynamics of the larger scales of motion. Anisotropy in the homogeneous $xy$-plane due to the initial conditions persists as $\overline{u'^2} \neq \overline{v'^2} \neq \overline{w'^2}$.

A possible explanation for the underestimation of $\overline{w'^2}$ in the DNS is as follows. The nonlinear advection term in the Navier–Stokes equation can be written in wave number space as [$\mathcal{F}(\cdot)$ denotes the Fourier transform]

$$\mathcal{F}\left[\frac{\partial}{\partial x_j}(u_i\,u_j)\right] = i\,k_j\,\mathcal{F}(u_i\,u_j)\ , \tag{26}$$

where $\mathcal{F}(u_i\,u_j) = \sum_{\mathbf{k}'} \widehat{u}_i(\mathbf{k}')\widehat{u}_j(\mathbf{k}-\mathbf{k}')$.[26] Accordingly, energy is transferred from wave vectors $\mathbf{k}'$ and $\mathbf{k}'' = \mathbf{k} - \mathbf{k}'$, which are supported on the discrete numerical grid, to wave vector $\mathbf{k}$, which may or may not be supported on the grid. This is analogous to the supergrid, cross, or subgrid scale triadic interactions investigated using filtered data from a DNS of Rayleigh–Taylor mixing.[48] When the magnitude of the wave vector satisfies $|\mathbf{k}| < \pi\Delta x$, the triadic wave vector interaction supplies energy to a scale too small to be supported on the grid and aliasing errors are generated. If properly resolved, this energy transfer is negligible and numerical

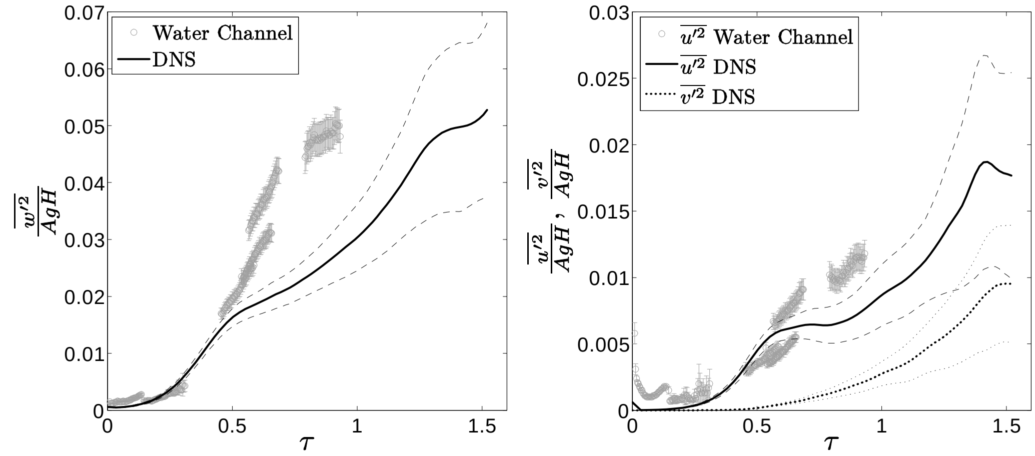

FIG. 12: Evolution of normalized vertical velocity variance (left) and horizontal velocity variances (right) on the centerplane ($z = 0$) of the mixing layer from the DNS and the water channel experiment. Uncertainty estimates (95% confidence interval bounds) are denoted by dashed and dotted lines.

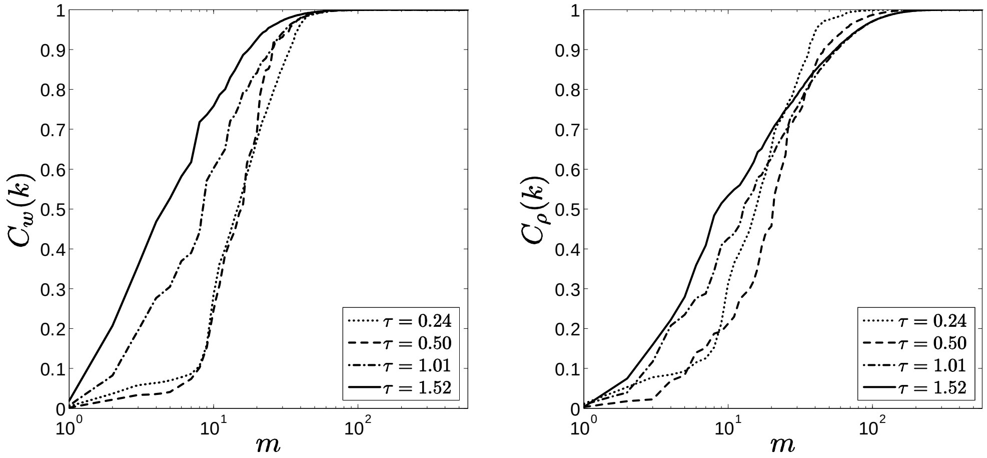

FIG. 13: Cumulative energy distributions of the vertical velocity variance spectrum (left) and density variance spectrum (right) on the centerplane ($z = 0$) of the mixing layer from the DNS at various dimensionless times.

filters are used to eliminate the influence of aliasing errors on the solution. At the other end of the spectrum, if $|\mathbf{k}| > 2\pi/L_x$ or $|\mathbf{k}| > 2\pi/L_y$, then energy from wave vectors $\mathbf{k}'$ and $\mathbf{k}''$ is transferred to a wavelength too large to be supported by the numerical domain. In this case, the energy is lost entirely. Thus, two resolution criteria should be satisfied for fully-resolving a DNS of any experiment: (1) the grid resolution must be fine enough to prevent the loss of energy to scales too small to be resolved, causing aliasing errors, and; (2) the domain must be large enough to permit creation of successively longer wavelengths through triadic interactions of the larger scales of motion. Thus, the domain size must be large enough to minimize the loss of energy to modes not supported by the discrete grid. These criteria are loosely satisfied with the current domain size and are further explored below.

In order to satisfy the first resolution requirement, the grid spacing must be the same size or smaller than the smallest dynamic scale in the flow. While this first requirement can typically be satisfied *a priori*, the second requirement may not be for Rayleigh–Taylor mixing simulations. The large-scale resolution requirement implies that the energy in the largest scales (low wavenumber regime of the spectrum) must constitute only a fraction of the total energy of the flow. Here, the normalized cumulative energy spectra

$$C_\phi(k) = \frac{\int_0^k E_\phi(k')\,\mathrm{d}k'}{\int_0^\infty E_\phi(k')\,\mathrm{d}k'} \qquad (27)$$

are examined, which provide a measure of the cumulative energy in the spectrum of $\phi$ from mode 1 to mode $m = 2\pi/k$. If the spectrum of fluctuations for a given scalar is fully-resolved, including the small-wavenumber peak of the energy spectrum, then

$$\lim_{k\to 0}\frac{\mathrm{d}C_\phi(k)}{\mathrm{d}k}\approx 0\,. \tag{28}$$

If Eq. (28) is not satisfied, then the peak of the energy spectrum is not fully resolved and the energy transfer to larger scales is not negligible. The normalized cumulative energy spectra for the vertical velocity fluctuations and density fluctuations on the centerplane are shown in Fig. 13. At early times, $\tau < 0.5$, the slopes of $C_w(k)$ and $C_\rho(k)$ at $m = 1$ (*i.e.* $k = 2\pi/L_x$) are small. However, beyond $\tau \approx 0.5$, this criterion is not satisfied, especially for the vertical velocity variance spectrum. Thus, the discrepancy between the DNS and the experimentally-measured values of $\overline{w'^2}$ beyond $\tau \approx 0.5$ is due to the fact that the full dynamic range of $E_w(k)$ is not resolved.

### F. One-dimensional energy spectra

The velocity variance evolution shown in Figs. 12 can be further examined by comparing the centerplane vertical velocity variance spectra at various times shown in Fig. 14 (the spectra shown in Figs. 14 and 15 are normalized using $\lambda_* = 0.661$ cm and $k_* = 9.51$ cm$^{-1}$). Caution must be exercised when comparing experimental spectra measured using a one-dimensional 'flying-wire' technique[26] and spectra from the DNS calculated using annular summations of energy within wave number rings. The experimentally-measured spectra contain additional low-wave number energy content from wave vectors not aligned with the $x$-axis. This spectral information cannot be distinguished or removed from the signal in a one-dimensional measurement.[26] However, it is possible to recreate an analogous spectrum from the two-dimensional spectrum calculated from the DNS. Beginning with the two-dimensional Fourier transform of a scalar field $\phi$,

$$\widehat{\phi}(k_x,k_y) = \frac{1}{L_xL_y}\int_0^{L_x}\int_0^{L_y}\phi(x,y)\,\mathrm{e}^{-i(k_xx+k_yy)}\,\mathrm{d}y\,\mathrm{d}x\,, \tag{29}$$

the energy content may be calculated by

$$E_\phi(k_x,k_y) = \frac{\left|\widehat{\phi}(k_x,k_y)\right|^2}{2}\,. \tag{30}$$

The analogous one-dimensional spectrum in the $x$-direction can be calculated by adding the off-axis energy content to the appropriate $k_x$ wave number,

$$E^*_\phi(k_x) = \frac{2}{\Delta k_x}\sum_{k_y=-\pi/L_y}^{\pi/L_y} E_\phi(k_x,k_y)\,. \tag{31}$$

As the Reynolds number of the mixing layer increases, a broader spectrum of velocity and density scales develops. A comparison of the one-dimensional vertical velocity variance spectra from the DNS and the water channel experiment is shown in Fig. 14. For the overlapping

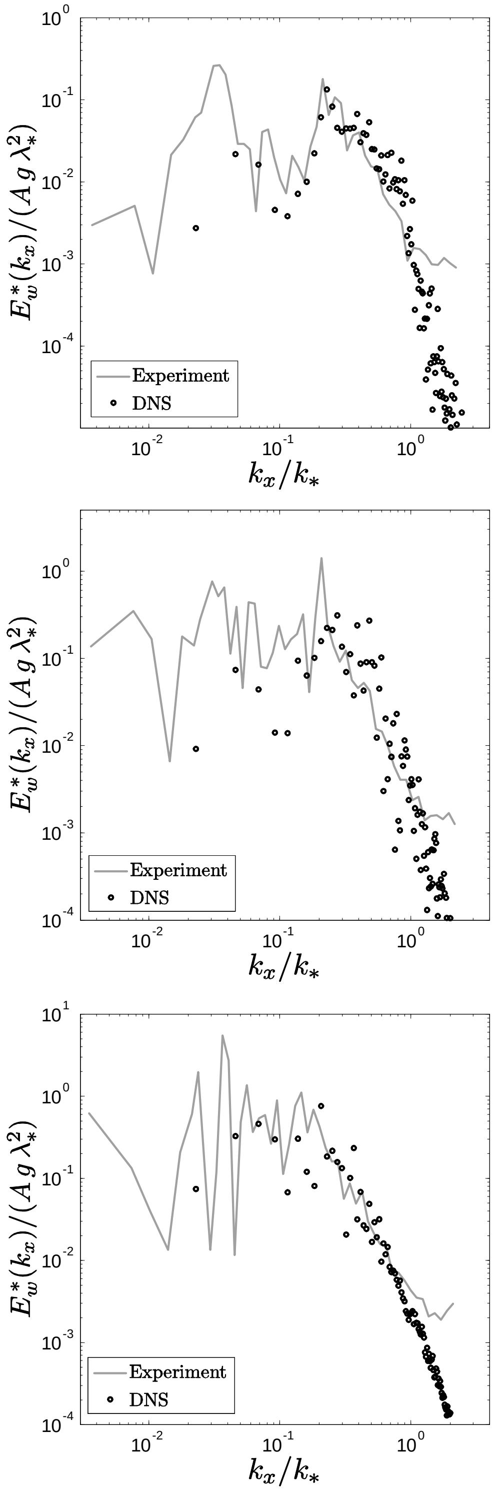

FIG. 14: Comparison of the normalized one-dimensional vertical velocity variance spectra $E^*_w(k_x)$ from the DNS and the water channel experiment on the centerplane ($z = 0$) of the mixing layer at $\tau = 0.31$ (top), $\tau = 0.58$ (middle), and $\tau = 0.92$ (bottom).

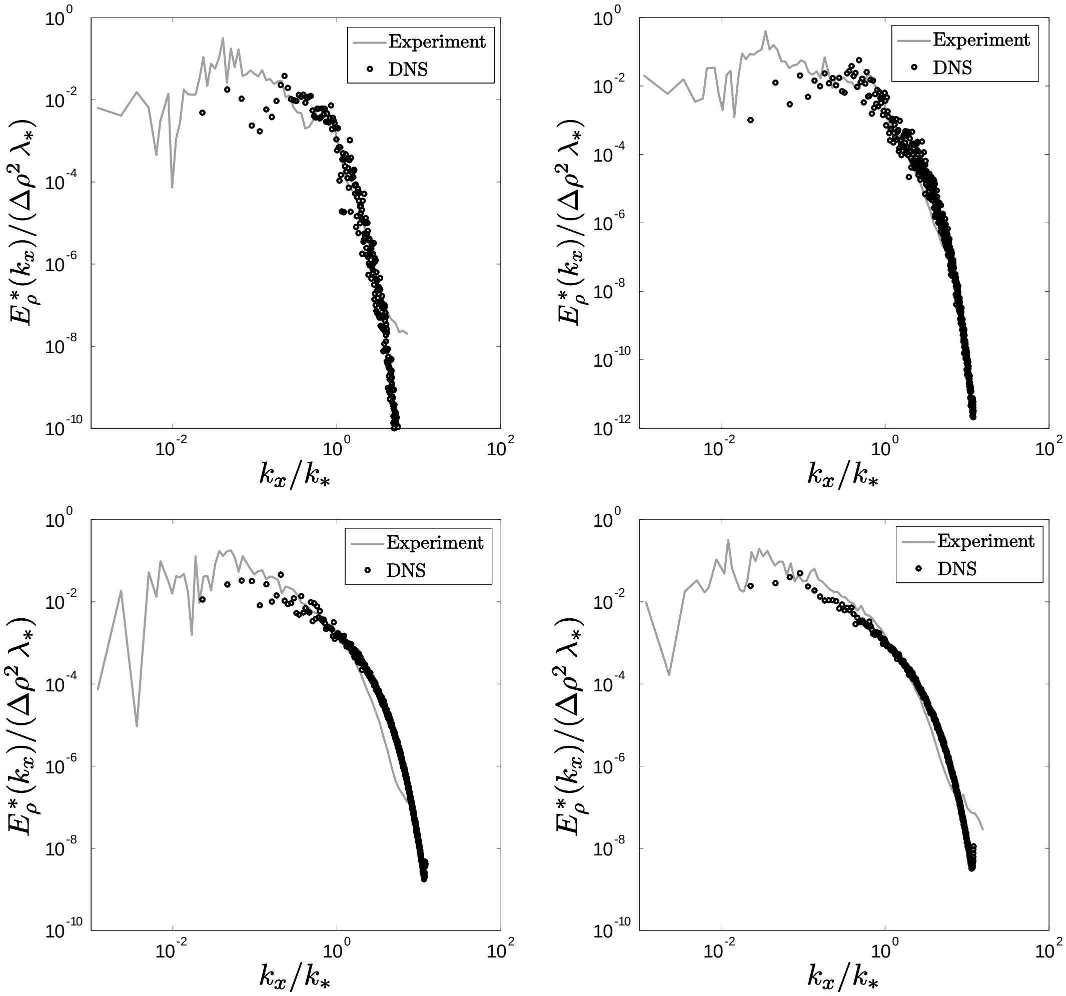

FIG. 15: Comparison of the normalized one-dimensional density variance spectrum $E_\rho^*(k_x)$ from the DNS and the water channel experiment on the centerplane ($z = 0$) of the mixing layer at $\tau = 0.17$ (top left), $\tau = 0.4$ (top right), $\tau = 0.87$ (bottom left), and $\tau = 1.36$ (bottom right).

range of wave numbers, the DNS and the experiment exhibit good agreement. The largest discrepancy is seen in the longest wavelengths in the DNS. As shown in Fig. 13, the domain size $L_x = 28.8$ cm limits the resolution of the long wavelength content in the initial vertical velocity spectrum and the energy transfer among the largest scales. Thus, the DNS model of the experiment well-represents the mixing layer dynamics with the exception of the longest wavelengths, *i.e.* modes 1 and 2. In order to better resolve wavelengths $\lambda \approx 15$–$30$ cm, the domain size in the $x$-direction must be increased four- to eight-fold.

A similar comparison of the centerplane density variance spectrum can be made, where a similar procedure is used to calculate a one-dimensional spectrum from the DNS. The comparison of $E_\rho^*(k_x)$ from the DNS and the experiment is shown in Fig. 15. Again, the longest wavelengths in the DNS exhibit less energy than the experimentally-measured spectra. As shown by the cumulative energy spectrum in Fig. 13, the total amount of energy in the first two modes accounts for less than 5% of the total density variance at early times ($\tau \leq 1$). Thus, the inability of the DNS to fully resolve the dynamics of the lowest two modes has little effect on the value of $\overline{\rho'^2}$. At the latest time in the simulation ($\tau = 1.52$), the energy deficit in the longest wavelengths in the DNS remains; however, as shown in Fig. 13, the energy content in the first two modes is greater than 5% of the total variance. Thus, to better resolve the late-time mixing dynamics, a larger domain size in the $x$-direction is required.

### G. Molecular mixing parameter

In addition to fluctuating velocity statistics, the degree of molecular mixing is also compared and shows favorable agreement between the DNS and the experiment. The evolution of the molecular mixing parameter[49] (see Ref.

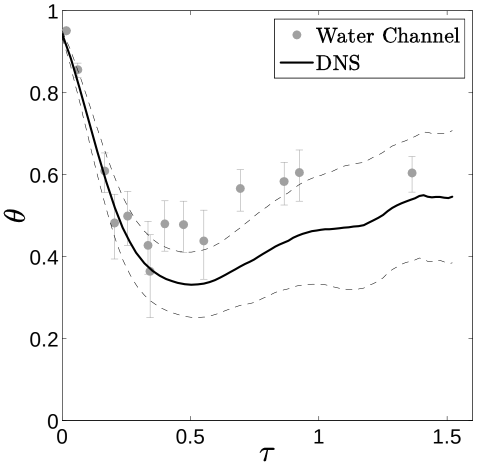

FIG. 16: Evolution of $\theta$ on the centerplane ($z = 0$) of the mixing layer from the DNS and the water channel experiment. Uncertainty estimates (95% confidence interval bounds) are denoted by dashed lines.

17 for a complete discussion)

$$\theta(z,t) = 1 - \frac{\overline{\rho'^2}}{\left(\rho_1 - \rho_2\right)^2\, \overline{f}_1\, \overline{f}_2} = 1 - \frac{\overline{f_1'^2}}{\overline{f}_1\, \overline{f}_2} \tag{32}$$

on the centerplane of the mixing layer is shown in Fig. 16. Both the DNS and the experiment show the same dynamic trend of a decreasing $\theta$ at early times, followed by a slow rise to an approximately late-time asymptotic value $\theta \approx 0.55$ in the experiment. Both exhibit minimum values $\theta \approx 0.35$–$0.45$ at similar times $\tau \approx 0.5$. While the DNS exhibits a systematically lower value of $\theta$ than reported in the experiment,[17] the uncertainties in the statistical measurements from the DNS and experiment overlap. The underestimation of $\theta$ in the DNS suggests that $\overline{f_1'^2}$ (or $\overline{\rho'^2}$) on the centerplane is overestimated in the DNS relative to the experiment. At the latest measurement time in the experiment, $\theta \approx 0.6$ from the DNS.

## VI. DISCUSSION AND CONCLUSIONS

A 1152×760×1280 spectral/compact difference DNS of a small Atwood number Rayleigh–Taylor driven mixing layer using physical parameters, computational geometry, and initial density and velocity perturbations approximating those in a hot/cold water channel experiment[17] was performed to examine the physical mixing processes in detail. As summarized in Sec. II, the present simulation differs in several important ways from previous simulations approximating experiments or from simulations using idealized initial conditions. To facilitate a comparison of DNS data to experimental measurements, a representation of the experimental initial perturbations measured just off of the splitter plate separating the water streams before they mix was used to seed the initial conditions in the DNS. Specifically, the multimode initial conditions measured using a combination of thermocouples, planar laser-induced fluorescence, and particle-image velocimetry in the experiment reported by Mueschke et al.[17] were parameterized for use in the DNS. These initial conditions include perturbations to the initial density field in both the $x$- and $y$-directions and perturbations to the initial velocity field. The procedure used to obtain and implement this parameterization was described in Sec. III and in the Appendix.

The DNS was validated by comparing integral-scale, turbulence, and mixing statistics with measurements from the water channel experiment. In addition to qualitative comparisons between the flow structure observed in the DNS and experiment, the bubble front mixing layer width $h_b$ and the self-similar growth parameter $\alpha_b$ were compared. The growth predicted by the DNS was in good agreement with the experimental measurements of the quadratic-in-time self-similar growth of $h_b(t)$ and $\alpha_b \approx 0.07$ at the latest time achieved. MILES simulations approximating Rayleigh–Taylor instability experiments have predicted values of $\alpha_b$ approximately 20% smaller than measured experimentally.[3,42]

Turbulence statistics obtained from the DNS were then compared with available data from the experiment. Estimates of the dominant wavelengths in the different coordinate directions, together with estimates of the number of turbulent structures over which statistics were computed, were first used to provide estimates of statistical uncertainty. The velocity variances on the centerplane of the mixing layer were compared between DNS and experiment: while all were in good agreement for early evolution times, the values from the simulation underestimated the variances at later times. From the cumulative energy distributions and phenomenology pertaining to triadic nonlinear interactions between modes that are not supported on the computational grid, this discrepancy was attributed to the finite domain size in the periodic directions. Accordingly, this DNS illustrates the base criteria required (both at the large and small scales) to fully resolve a Rayleigh–Taylor mixing layer experiment. In addition, one-dimensional vertical velocity variance and density variance spectra were in good agreement between the DNS and experiment for all times (for the modes supported on the computational grid). The evolution of the molecular mixing parameter on the centerplane $\theta$ qualitatively agreed with the experimental measurement over the entire simulation time; while $\theta$ from the DNS was lower than measured after the transition to a more turbulent state ($\tau \gtrsim 0.8$), the DNS values overlapped with the uncertainties in the measurements. At intermediate times ($0.5 < \tau < 1$), $\theta$ from the DNS was approximately 20% lower than the experimental values. However, at the latest time measured in the experiment ($\tau \approx 1.4$), $\theta \approx 0.6$ compared to $\theta \approx 0.55$ from the DNS.

This work demonstrates that a parameterization of the full experimentally-measured initial conditions can yield simulation data that quantitatively agrees well with experimentally-measured low- and higher-order statistics, such as mixing layer growth, molecular mixing parameters, variances, and energy spectra. Part II of this work discusses other quantities obtained from the DNS that are not available experimentally.

## APPENDIX: INITIAL CONDITIONS IMPLEMENTATION ISSUES

### 1. Relationship between initial interfacial perturbations and density fluctuations

In developing the initial conditions formulation in Eqs. (9) and (11), several issues arise which must be addressed. First, the initial interfacial perturbations in the $x$-direction $\widehat{\zeta}(k_x)$ must be inferred from the density fluctuation on the centerplane $\widehat{\rho}(k_x)$. To accomplish this, note that a relationship between $\widehat{\rho}(k_x)$ and $\widehat{\zeta}(k_x)$ exists, and relies on Eq. (6) as an adequate model for the initial density field and a constant $\varepsilon$. This parameterization assumes that diffusion occurs only in the $z$-direction, which is valid for $\widehat{\zeta}(k) \ll \lambda = 2\pi/k$. Also, when measuring density fluctuations at a distance $x = 0.5$ cm from the splitter plate, the hot and cold water streams have been in contact for the same amount of time and, thus, a constant $\varepsilon$ is plausible.

To relate $E_\rho(k_x)$ to $E_\zeta(k_x)$ in the $x$-direction using Eq. (6), the fluctuating density field on the centerplane can be expressed as a sum of Fourier modes,

$$\begin{aligned} \rho(x, z=0)' &= \rho(x, z=0) - \frac{\rho_1+\rho_2}{2} \qquad \text{(A.1)} \\ &= \sum_{k_x=k_{\min}}^{k_{\max}} \widehat{\rho}(k_x)\, \mathrm{e}^{ik_x x}\,. \end{aligned}$$

Substituting Eq. (A.1) into Eq. (6) evaluated at $z = 0$,

$$\sum_{k_x=k_{\min}}^{k_{\max}} \widehat{\rho}(k_x)\, \mathrm{e}^{ik_x x} = \frac{\rho_1-\rho_2}{2}\, \mathrm{erf}\left[\frac{\zeta(x)}{\varepsilon}\right], \qquad \text{(A.2)}$$

where the interfacial perturbation $\zeta(x, y)$ has been restricted to the $x$-axis. Consequently,

$$\zeta(x) = \varepsilon\, \mathrm{erf}^{-1}\left[\frac{2}{\rho_1-\rho_2} \sum_{k_x=k_{\min}}^{k_{\max}} \widehat{\rho}(k_x)\, \mathrm{e}^{ik_x x}\right]. \qquad \text{(A.3)}$$

The interfacial perturbation spectrum, $E_\zeta(k_x)$, can be computed by taking the one-dimensional Fourier transform of the reconstructed interfacial perturbation $\zeta(x)$ in Eq. (A.3). While this procedure is required to correctly implement the interfacial perturbation in the $x$-direction, the modeled spectrum $E_\zeta(k_x)$ is nearly identical to the measured spectrum $E_\rho(k_x)$.

### 2. Relationship between initial experimental and simulation spectra

Another issue arises because the numerical grid of the DNS is capable of supporting only a finite number of modes, where the total bandwidth is bounded by the total horizontal domain size $L_x \times L_y$. The corresponding minimum wave vector is $\mathbf{k}_{min} = (2\pi/L_x, 2\pi/L_y)$, and the maximum wave vector is determined by the grid resolution (Nyquist limit) $\mathbf{k}_{max} = (\pi/\Delta x, \pi/\Delta y)$. In general, the set of discrete wave numbers supported by the grid does not match the specific wave numbers at which the energy spectra are experimentally measured. Thus, a strategy is required to map the experimentally-measured energy values to the discrete wave numbers in the simulation.

To reduce this sensitivity of the DNS results on the choice of domain size, a novel strategy of implementing the experimental spectra was investigated. The initial spectra were formulated using a local integration over individual wavepackets of the experimental spectrum,

$$E_{sim}(k_i) = \frac{1}{\Delta k_i} \int_{k_i-\Delta k_i/2}^{k_i+\Delta k_i/2} E_{exp}(k_i')\, \mathrm{d}k_i'\,, \qquad \text{(A.4)}$$

where $\Delta k_i = 2\pi/L_i$. While the numerical grid resolution of the longer wavelengths remains the same, variations in the experimental spectral energy content may be captured robustly. This local wavepacket integration method yields more consistent results for small changes in the domain size, as opposed to simply interpolating energy values from the measured experimental spectra. Further details concerning these formulations are available elsewhere.[24]

## ACKNOWLEDGMENTS

The authors thank Dr. Malcolm J. Andrews for insightful comments concerning the experimental portion of this work, and Drs. Andrew W. Cook and William H. Cabot for providing their code. This work was performed under the auspices of the U.S. Department of Energy by Lawrence Livermore National Laboratory under Contract DE-AC52-07NA27344. A portion of this research was also sponsored by the National Nuclear Security Administration under the Stewardship Science Academic Alliances program through DOE Research Grant DE-FG03-02NA00060.

---

[1] D. L. Youngs, "Three-dimensional numerical simulation of turbulent mixing by Rayleigh-Taylor instability," Phys. Fluids A **3**, 1312 (1991).

[2] D. L. Youngs, "Numerical simulation of mixing by Rayleigh-Taylor and Richtmyer-Meshkov instabilities," Las. Part. Beams **12**, 725 (1994).

[3] P. F. Linden, J. M. Redondo, and D. L. Youngs, "Molecular mixing in Rayleigh-Taylor instability," J. Fluid Mech. **265**, 97 (1994).

[4] S. B. Dalziel, P. F. Linden, and D. L. Youngs, "Self-similarity and internal structure of turbulence induced by Rayleigh-Taylor instability," J. Fluid Mech. **399**, 1 (1999).

[5] G. Dimonte, D. L. Youngs, A. Dimits, S. Weber, M. Marinak, S. Wunsch, C. Garasi, A. Robinson, M. J. Andrews, P. Ramaprabhu, A. C. Calder, B. Fryxell, J. Biello, L. Dursi, P. MacNeice, K. Olson, P. Ricker, R. Rosner, F. Timmes, H. Tufo, Y.-N. Young, and M. Zingale, "A comparative study of the turbulent Rayleigh-Taylor instability using high-resolution three-dimensional numerical simulations: The Alpha-Group collaboration," Phys. Fluids **16**, 1668 (2004).

[6] A. W. Cook and P. E. Dimotakis, "Transition stages of Rayleigh–Taylor instability between miscible fluids," J. Fluid Mech. **443**, 69 (2001); Corrigendum, J. Fluid Mech. **457**, 410 (2002).

[7] A. W. Cook and Y. Zhou, "Energy transfer in Rayleigh-Taylor instability," Phys. Rev. E **66**, 026312 (2002).

[8] W. H. Cabot and A. W. Cook, "Reynolds number effects on Rayleigh–Taylor instability with possible implications for type-Ia supernovae," Nat. Phys. **2**, 562 (2006).

[9] Y.-N. Young, H. Tufo, A. Dubey, and R. Rosner, "On the miscible Rayleigh-Taylor instability: two and three dimensions," J. Fluid Mech. **447**, 377 (2001).

[10] J. R. Ristorcelli and T. T. Clark, "Rayleigh–Taylor turbulence: self-similar analysis and direct numerical simulations," J. Fluid Mech. **507**, 213 (2004).

[11] L. Wang, J. Li, and Z. Xie, "Large-eddy simulation of 3-dimensional Rayleigh-Taylor instability in incompressible fluids," Sci. China A **45**, 95 (2002).

[12] R. M. Darlington, T. L. McAbee, and G. Rodrigue, "Large eddy simulation and ALE mesh motion in Rayleigh-Taylor instability simulation," Comp. Phys. Comm. **144**, 261 (2002).

[13] A. W. Cook, W. Cabot, and P. L. Miller, "The mixing transition in Rayleigh-Taylor instability," J. Fluid Mech. **511**, 333 (2004).

[14] W. Cabot, "Comparison of two- and three-dimensional simulations of miscible Rayleigh–Taylor instability," Phys. Fluids **18**, 045101 (2006).

[15] P. Ramaprabhu, G. Dimonte & M. J. Andrews, "A numerical study of the influence of initial perturbations on the turbulent Rayleigh–Taylor instability," J. Fluid Mech. **536**, 285 (2005).

[16] P. Ramaprabhu and M. J. Andrews, "On the initialization of Rayleigh–Taylor simulations," Phys. Fluids **16**, L59 (2004).

[17] N. J. Mueschke, M. J. Andrews, and O. Schilling, "Experimental characterization of initial conditions and spatio-temporal evolution of a small Atwood Rayleigh–Taylor mixing layer," J. Fluid Mech. **567**, 27 (2006).

[18] N. J. Mueschke and O. Schilling, "Investigation of Rayleigh–Taylor turbulence and mixing using direct numerical simulation with experimentally-measured initial conditions. II. Dynamics of transitional flow and mixing statistics," Phys. Fluids (2008).

[19] P. F. Linden and J. M. Redondo, "Molecular mixing in Rayleigh-Taylor instability. Part 1: Global mixing," Phys. Fluids A **3**, 1269 (1991).

[20] D. M. Snider and M. J. Andrews, "Rayleigh–Taylor and shear driven mixing with an unstable thermal stratification," Phys. Fluids A **6**, 3324 (1994).

[21] P. N. Wilson, "An investigation into the spectral evolution of turbulent mixing by Rayleigh–Taylor instability," Ph.D. thesis, Texas A&M University (2002).

[22] P. Ramaprabhu, "On the dynamics of Rayleigh–Taylor mixing," Ph.D. thesis, Texas A&M University (2003).

[23] N. J. Mueschke, "An investigation of the influence of initial conditions on Rayleigh–Taylor mixing," M.S. thesis, Texas A&M University (2004).

[24] N. J. Mueschke, "Experimental and numerical study of molecular mixing dynamics in Rayleigh–Taylor unstable flows," Ph.D. thesis, Texas A&M University (2008).

[25] G. I. Taylor, "The spectrum of turbulence," Proc. Royal Soc. London A **164**, 476 (1938).

[26] S. B. Pope, *Turbulent Flows* (Cambridge University Press, New York, 2000).

[27] P. G. Drazin and W. H. Reid, *Hydrodynamic Stability*, second edition (Cambridge University Press, New York, 2004).

[28] D. D. Joseph, "Fluid dynamics of two miscible liquids with diffusion and gradient stress," Eur. J. Mech. B **9**, 565 (1990).

[29] D. L. Sandoval, "The dynamics of variable density turbulence," Ph.D. thesis, University of Washington (1995).

[30] R. C. Cook, R. L. McEachern, and R. B. Stephens, "Representative surface profile power spectra from capsules used in Nova and Omega implosion experiments," Fus. Sci. Tech. **35**, 224 (1999).

[31] M. M. Rogers and R. D. Moser, "Direct simulation of a self-similar turbulent mixing layer," Phys. Fluids **6**, 903 (1994).

[32] C. Canuto, M. Y. Hussaini, A. Quarteroni, and T. A. Zang, *Spectral Methods: Fundamentals in Single Domains*, Series in Scientific Computation (Springer-Verlag, New York, 2006).

[33] S. K. Lele, "Compact finite difference schemes with spectral-like resolution," J. Comput. Phys. **103**, 16 (1992).

[34] G. Dimonte, P. Ramaprabhu, D. L. Youngs, M. J. Andrews, and R. Rosner, "Recent advances in the turbulent Rayleigh–Taylor instability," Phys. Plasmas **12**, 056301 (2005).

[35] S. Chandrasekhar, *Hydrodynamic and Hydromagnetic Stability* (Dover, New York, 1961).

[36] K. Kadau, C. Rosenblatt, J. L. Barber, T. C. Germann, Z. Huang, P. Carlès, and B. J. Alder "The importance of fluctuations in fluid mixing," Proc. Nat. Acad. Sci. **104**, 7741 (2007).

[37] J. L. van Ingen, "A suggested semi-empirical method for the calculation of boundary layer transition regime," Inst. of Tech., Dept. of Aeronautics and Engineering Report VTH-74, Delft, Holland (1956).

[38] A. M. O. Smith and N. Gamberoni, "Transition, pressure gradient, and stability theory," Proc. Ninth Internat. Cong. Appl. Mech. **4**, 234 (1957).

[39] D. Laney, P.-T. Bremer, A. Mascarenhas, P. Miller, and V. Pascucci, "Understanding the structure of the turbulent mixing layer in hydrodynamic instabilities," IEEE Trans. Vis. Computer Graphics **12**, 1053 (2006).

[40] S. W. Haan, "Onset of nonlinear saturation for Rayleigh-Taylor growth in the presence of a full spectrum of modes," Phys. Rev. A **39**, 5812 (1989).

[41] D. L. Youngs, "Numerical simulation of turbulent mixing by Rayleigh-Taylor instability," Physica D **12**, 32 (1984).

[42] P. Ramaprabhu and M. J. Andrews, "Experimental investigation of Rayleigh-Taylor mixing at small Atwood numbers," J. Fluid Mech. **502**, 233 (2004).

[43] N. N. Anuchina, Yu. A. Kucherenko, V. E. Neuvazhaev, V. N. Ogibina, L. I. Shibarshov, and V. G. Yakovlev, "Turbulent mixing at an accelerating interface between liquids of different density," Fluid Dyn. **6**, 916 (1978).

[44] D. Shvarts, U. Alon, D. Ofer, R. L. McCrory, and C. P. Verdon, "Nonlinear evolution of multimode Rayleigh–Taylor instability in two and three dimensions," Phys. Plasmas **2**, 2465 (1995).

[45] A. Rikanati, D. Oron, U. Alon, and D. Shvarts, "Statistical mechanics merger model for hydrodynamic instabilities," Astrophys. J. Suppl. **127**, 451 (2000).

[46] L. H. Benedict and R. D. Gould, "Towards better uncertainty estimates for turbulence statistics," Exp. Fluids **22**, 129 (1996).

[47] G. K. Batchelor, *The Theory of Homogenous Turbulence* (Cambridge University Press, Cambridge, 1953).

[48] W. H. Cabot, O. Schilling, and Y. Zhou, "Influence of subgrid scales on resolvable turbulence and mixing in Rayleigh–Taylor flow," Phys. Fluids **16**, 495 (2004).

[49] P. V. Danckwerts, "The definition and measurement of some characteristics of mixtures," Appl. Sci. Res. **3**, 279 (1952).